Applied Acoustics 240 (2025) 110896

Contents lists available at ScienceDirect

Applied Acoustics

journal homepage: www.elsevier.com/locate/apacoust

Experimental assessment of a programmable Electroacoustic Liner in a representative turbofan facility

E. De Bono [a,*], E. Salze [b], M. Collet [a], M. Gillet [c], M. Ouisse [c], M. Volery [d], H. Lissek [d], J. Mardjono [e]

[a] Univ. Lyon, École Centrale de Lyon, LTDS UMR 5513, F-69134 Ecully, France
[b] Univ. Lyon, École Centrale de Lyon, LMFA UMR 5509, F-69134 Ecully, France
[c] SUPMICROTECH, Université de Franche-Comté, CNRS, institut FEMTO-ST, F-25000 Besançon, France
[d] Signal Processing Laboratory LTS2, Ecole Polytechnique Fédérale de Lausanne, Station 11, CH-1015 Lausanne, Switzerland
[e] Safran Aircraft Engines, F-75015, Paris, France

ARTICLE INFO

Keywords:
Acoustic liner
Turbofan noise
Electroacoustic resonator
Electroacoustic liner
Impedance control
Programmable boundary

ABSTRACT

The Flightpath 2050 European Union stringent regulations for aviation noise reduction, along with the new generation of Ultra-High-Bypass-Ratio turbofans to reduce fuel consumption, significantly challenge the scientific community to find unprecedented acoustic liner designs. The SALUTE H2020 project has taken up this challenge, by designing and testing a programmable metasurface made up of electroacoustic resonators. Each electroacoustic resonator is composed by a loudspeaker and four microphones in a compact design, allowing to synthesize tunable local impedance behaviours thanks to a current-driven control strategy. A steel wiremesh mounted onto a perforated plate allows to protect the elctromechanical devices from the aerodynamic disturbances. For the first time, such advanced liner concept has been tested in a scaled turbofan rig: the ECL-B3 PHARE-2 in the Laboratory of Fluid Mechanics and Acoustics of the Ecole Centrale of Lyon. The performances of the electroacoustic liner reported in this paper, correspond to three different regimes: 30%, 40% and 100% of the nominal engine speed. The electroacoustic technology demonstrated robustness faced with a realistic reproduction of actual turbofan conditions, as well as its tunability to target different frequency bandwidth, attaining good radiated noise reduction. The results reported in this experimental campaign open the doors for unprecedented liner designs, by exploiting the huge potentialities of programmable surfaces.

1. Introduction

The aircraft engines must face, on the one hand, significant restrictions on fuel consumptions and pollutant emissions, and on the other hand increasingly stringent regulations on noise pollution [1]. These two constraints are unfortunately in conflict with each other. As the fuel restrictions demand larger turbofan diameters, less number of blades, higher by-pass-ratios and shorter nacelles (leaving less available space for acoustic lining treatments), the engine noise signature is shifted toward lower frequencies, which are much more challenging to mitigate than high frequencies. It is the case of the Ultra-High-Bypass-Ratio (UHBR) turbofans, whose implementation has been prompting a large amount of research projects in the quest toward innovative acoustic liner concepts [2], exploiting multiple quarter-wavelength or Helmholtz resonators [3,4] often combined with micro-perforated-plates [5–7], or based upon flexible membranes [8,9]. Nevertheless, very few designs have actually been validated on test-rigs representative of actual turbofan engines. This paper focuses on acoustic liner application at the inlet of the turbofan nacelle. The analytical work E. J. Rice about optimal impedance design criteria [10,11] applied to spinning modes, for liners made up of perforated sheets and back-cavities, led to significant noise attenuation at the targeted Blade-Passing-Frequency (BPF), for a ratio of the liner length over the nacelle internal diameter $L/D = 1$. The ratio L/D along with the thickness-to-diameter ratio d/D, are those which must be minimized to comply with the spatial constraints in the nacelle. A longer and thicker liner clearly provides higher noise control efficiency, for this reason the above geometric parameters are specified, whenever available, for each significant acoustic liner of the state-of-art. Substantial experimental campaigns have been conducted at the NASA Glenn Research Center [12] on both passive and active tech-

* Corresponding author.
E-mail address: emanueledeb88@hotmail.it (E. De Bono).

https://doi.org/10.1016/j.apacoust.2025.110896
Received 12 February 2025; Received in revised form 21 May 2025; Accepted 12 June 2025
Available online 18 June 2025

nologies. While the first ones are currently employed in the aeronautic sector for their technological relative simplicity and robustness to comply with the strict aeronautical certification policies, the second ones offer very attractive potentialities in terms of tunability (to suppress tones at different flight stages) and efficiency at low frequencies [13]. Among the passive liners, in [14], single-degree-of-freedom (SDOF) and 3-degrees-of-freedom liners, were designed based upon numerical optimal impedance spectra and was characterized by $d/D = 0.14$, and $L/D = 1$. The highest sound pressure level (SPL) attenuation of about 12 dB was achieved at the first BPF (3 kHz), measured on a far-field microphone placed at an angle of 51.4° with respect to the nacelle longitudinal axis. The broadband noise, instead, was attenuated of maximum 3 dB. Recently, an additive manufactured liner composed of a perforated surface and backing cavities with horizontal and diagonal septa was optimized to low geometric ratios $L/D \approx 0.2$ and $d/D \approx 0.04$, and achieved an exceptional attenuation of 18.6 dB on the SPL of the first harmonic tone (960 Hz) on a far-field microphone at 43.5° with respect to the longitudinal axis. However, the attenuation in terms of acoustic Power Level (PWL) (computed on the area covered by the microphones arc surrounding the nacelle) at the same tone, did not overcome 2 dB. Among nonlocally-reacting liners [15,13] tested on the Advanced Noise Control Fan facility, we mention the Herschel-Quincke tubes [16,17] achieving about 8.6 dB of PWL attenuation at the targeted BPF, and up to 3 dB of PWL attenuation on the broadband noise, for a $L/D = 1$, and the spiralling liner [18] accomplishing interesting modal attenuations for a $L/D = 1$. The Advanced Noise Control Fan facility has also hosted various active concepts, such as Helmholtz resonators backed by electrodynamic loudspeakers, achieving significant noise attenuation at the BPF, but complex non-collocated architecture (with dislocated resonators and error microphones) required an excessive ratio L/D. The German Aerospace Center facility also hosted active control strategies, such as the one proposed in [19], involving large values of L/D, though only 3 dB of noise attenuation was achieved at the BPF. In [20], actuators and sensors required a $L/D \approx 1.5$, and a noise attenuation up to 15 dB was achieved at the BPF, along some specific radiation angles. Another interesting active-noise-cancellation (ANC) technique, consisting in generating out-of-phase spinning modes, was proposed in [21], and achieved up to 13 dB of noise attenuation at the BPF, for a $L/D = 0.5$.

The performances and the corresponding geometric ratios listed above for the innovative liner technologies tested on representative turbofan test-rigs, serve as a benchmark for assessing the potentialities of our electroacoustic liner (EL) concept. An EL is composed of Electroacoustic Resonators (ERs), whose local impedance can be programmed. The idea stems from the seminal work of Olson and May [22], leading to various declinations of the ER [23–26], up to the most robust pressure-based current-driven architecture [27]. This latter employs one or more microphones nearby the speaker, and a model-inversion digital control algorithm [28–33] to target the desired impedance by driving the electrical current in the speaker coil. Contrary to ANC strategies, the impedance control targets an acoustically passive behaviour of the treated boundary in the operative bandwidth. As acoustical passivity is sufficient condition for stability, independently of the external acoustic environment [34], the impedance control results to be more suitable than classical ANC, for applications in a highly aleatoric aeroacoustic domain, such as a turbofan nacelle. Observe that a liner is defined as acoustically passive if the average acoustic intensity at the interface between the liner and the air-cavity in the duct, travels from the air-cavity towards the liner [35]. In the specific case of locally-reacting liners [15] characterized by a classical impedance operator, the acoustical passivity condition translates into a positive real part of the impedance operator written in frequency-domain [36]. Notice that an active impedance control of liner is usually active from the electrical point of view, but it is designed to target passive acoustical impedances of the liner (in the sense of [36]), from which the importance to differentiate between electrical and acoustical passivity [28].

In the last years, the EL has proven to achieve significant isolation performances in rectangular cross-section waveguides [37,38] and with flow [39]. Such preliminary test-benches allowed to improve the overall design of our ERs, up to the SALUTE H2020 project, where the noise radiated from a representative turbofan test-rig was finally targeted. For the first time, the EL concept has been tested in the inlet of a realistic turbofan test-rig, the ECL-B3 (PHARE-2), allowing to assess the EL Technology Readiness Level (TRL) up to 3. Preliminary results have been shown in [40–46,39,47–50].

The objective of this paper is a thorough analysis of the experimental campaign on the PHARE-2 test-bench, carried out to prove the robustness of the EL when confronted to a representative turbofan environment, as well as to test its tunability in attenuating noise at various Blade-Passing-Frequencies and low-frequency harmonics.

The EL architecture and the control algorithm are resumed in Section 2.1, while in Section 2.2, the experimental setup employed on the ECL-B3 (PHARE-2) fan test-rig is described. Then, the achieved performances in terms of total, tonal and broadband noise attenuation are discussed in Section 3. The EL is tested against three engine speed regimes: $0.3N_n$, $0.4N_n$ and N_n, presented in Sections 3.1, 3.2 and 3.3, respectively (where N_n is the nominal engine speed of the PHARE-2 turbofan), demonstrating the tunability of our EL to attenuate different noise components and bandwidths. The value of N_n and the corresponding BPF is not disclosable for confidential reasons. Observe that, the lower regimes, such as $0.3N_n$ and $0.4N_n$, other than being representative of the flight approach conditions, are also interesting because their BPF is located at lower frequencies, which are closer to those actually excited by full size turbofan engines at their operative regimes. An overall discussion of the results is reported in Section 4, while the conclusions and next steps to further increase the potentials of such cutting edge technology, are given in Section 5.

All the acronyms and symbols employed in this paper are listed in Appendixes C and D, respectively.

2. Methodology

Here, we present first the liner configuration (in Section 2.1), outlining the ER technology and its control architecture. Then, in Section 2.2, we present the turbofan test-bench where the EL is tested, while in Section 2.3, the test-conditions relative to the different engine regimes are given.

2.1. Liner configuration

The EL is composed by ERs. Each ER is composed by a loudspeaker, 4 corner microphones (see Fig. 1a), for a front face of 5 cm × 5 cm, and a thickness of $d = 5$ cm. The 4 microphones in each ER retrieve an average estimation of the sound pressure on the speaker diaphragm. Hence, the desired impedance is achieved by reaching the corresponding velocity on the loudspeaker diaphragm, by piloting the electrical current (the controller variable) in the speaker coil. The control transfer function between the measured pressure and the electrical current is written based upon the loudspeaker SDOF model, given in Eq. (1) in terms of the Laplace variable s.

$$Z_0(s)\bar{v}(s) = \bar{p}(s) - \frac{Bl}{S_e}\bar{i}(s). \tag{1}$$

In Eq. (1), $\bar{p}(s)$ and $\bar{v}(s)$ are the acoustic pressure and velocity, respectively, on the speaker diaphragm, $\bar{i}(s)$ is the electrical current in the speaker coil, $Z_0(s) = M_0 s + R_0 + K_0/s$ is the acoustical impedance of the loudspeaker in open circuit, with M_0, R_0 and K_0 the corresponding acoustical mass, resistance and stiffness. The electrical current $\bar{i}(s)$ is multiplied by the force factor Bl to get the electromagnetic force, and divided by the effective area S_e to retrieve an equivalent pressure. Eq. (1) is the classical Thiele-Small SDOF model [51], whose parameters

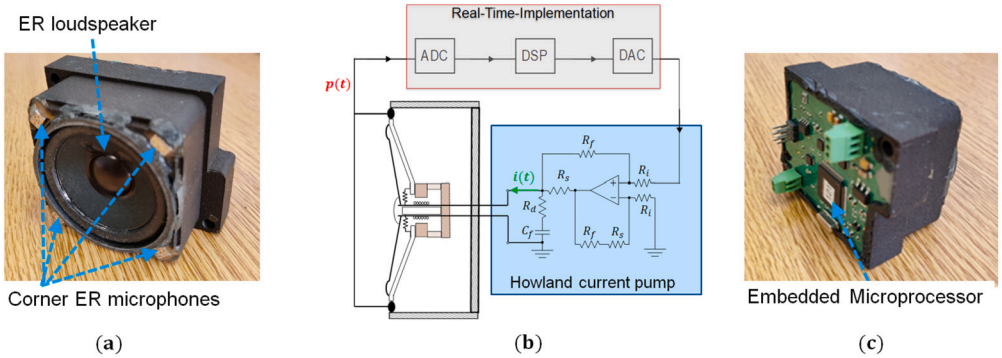

Fig. 1. Sketch of the controller architecture **(b)**, with frontal **(a)** and back-side **(b)** photos of an ER.

must be identified in order to properly synthesize the corrector transfer function. On the loudspeaker Thiele-Small parameters identification, we refer the reader to [28,39,52].

Observe that the impedance description of Eq. (1) is a lumped-element model corresponding to the first piston-like mode of the loudspeaker. The lumped-element model is valid as long as the sound pressure can be considered uniform on the ER, i.e. for wavelengths sufficiently larger than the lateral size of the ER. Nevertheless, in the control transfer function derived below, the pressure input around the speaker is averaged thanks to the four corner microphones, allowing to minimize the effect of non-uniform pressure distribution, and further extend the validity of the lumped-element model of Eq. (1) [37,39]. However, the upper frequency of validity of the lumped-element model is also limited by the arising of higher-order vibrational modes of the speaker at about 2.5 kHz. When approaching this frequency, the SDOF model (corresponding to the loudspeaker first mode) is insufficient to describe the speaker dynamics, and Eq. (1) loses its validity. In the current application, the frequency range targeted by the ERs do not overcome 1.5 kHz, allowing to employ Eq. (1) for the synthesis of the control transfer function by model-inversion strategy [28,29].

Hence, the expression of the electrical current $\bar{i}(s)$ as function of the measured pressure $\bar{p}(s)$, to reach a desired acoustic impedance $Z_d(s)$, can be written as:

$$\bar{i}(s) = H_{\mathrm{Loc}}(s)\bar{p}(s), \tag{2a}$$

$$H_{\mathrm{Loc}}(s) = \frac{S_e}{Bl}\left(1 - \frac{Z_0(s)}{Z_d(s)}\right). \tag{2b}$$

Further details about the model-inversion control synthesis can be found in [27,53,28,39,29,38], along with its efficiency in achieving the desired impedance $Z_d(s)$, in both normal and grazing incidence scenarios characterized by the plane wave regime (as the impedance tube). The real-time implementation of the electrical current defined in Eq. (2) is accomplished by classical Infinite Impulse Response (IIR) algorithm [34]. Each ER is controlled autonomously, and the control architecture is illustrated in Fig. 1b: the pressure signal, after being digitally converted by the analogue-digital-converter (ADC), is fed into a programmable digital-signal-processor (DSP) where the output of the control is computed at each time step. The Howland current pump [54] allows to enforce the electrical current i in the speaker coil independently of the voltage at the loudspeaker terminals. It consists of an operational amplifier, two input resistors R_i, two feedback resistors R_f, and a current sense resistor R_s. The resistance R_d and capacitance C_f constitutes the compensation circuit to ensure stability with the grounded load [55]. The digital processing instructions are downloaded on the embedded microprocessor (shown in Fig. 1c) from an external interface communicating directly with the user laptop, where the desired control law is defined.

The desired impedance $Z_d(s)$ can be a SDOF impedance with tunable coefficients in order to target the desired frequency range and with a suitable resistance. The general expression of the desired SDOF impedance is given in Eq. (3):

$$Z_{d,\mathrm{SDOF}}(s) = M_d s + R_d + \frac{K_d}{s}, \tag{3}$$

where $R_d = r_d \rho_0 c_0$ is the desired resistance, while the desired reactive components are defined as $M_d = \mu_M M_0$ and $K_d = \mu_K K_0$. As the mass term mainly determines both the bandwidth and the passivity margin of the ER [28], the μ_M coefficient can be adjusted to maximize the performances. The target stiffness coefficient μ_K, instead, is defined in order to tune the ER resonance at the targeted frequency f_d, which is given by:

$$f_d = f_0\sqrt{\frac{\mu_K}{\mu_M}}, \tag{4}$$

where $f_0 = (1/2\pi)\sqrt{K_0/M_0}$ is the resonance frequency of the ER in open circuit. Finally, the resistance coefficient r_d is chosen in order to achieve highest attenuation levels and preserve acoustical passivity [28]. In the results reported in Section 3, the target impedance will be identified by the parameters r_d, μ_M and f_d. From μ_M, f_d and f_0, μ_K can be directly obtained by Eq. (4) as $\mu_K = \mu_M\left(\frac{f_d}{f_0}\right)^2$, allowing to target a desired frequency f_d for any value of μ_M. Moreover, in the interpretation of the experimental results provided in Section 3, an important role is played by the quality-factor Q, defined as:

$$Q = \frac{\sqrt{M_d K_d}}{R_d} = \frac{\sqrt{\mu_M \mu_K}}{r_d}\frac{\sqrt{M_0 K_0}}{\rho_0 c_0} = \frac{\sqrt{\mu_M \mu_K}}{r_d} Q_0, \tag{5}$$

where we have called $Q_0 = \frac{\sqrt{M_0 K_0}}{\rho_0 c_0}$. Clearly, increasing the reactance components, or reducing the resistance leads to a higher quality factor.

In Eq. (3), the target impedance is a SDOF one, but the controller Eq. (2) is capable of accomplishing multi-degree-of-freedom impedances on each ER, as experimentally demonstrated in [56]. In the present work, we have targeted equivalent Double-Degrees-Of-Freedom (DDOF) impedances given by Eq. (6):

$$Z_{d,\mathrm{DDOF}}(s) = \left(\frac{1}{Z^{(1)}_{d,\mathrm{SDOF}}(s)} + \frac{1}{Z^{(2)}_{d,\mathrm{SDOF}}(s)}\right)^{-1}, \tag{6}$$

where $Z^{(1)}_{d,\mathrm{SDOF}}$ and $Z^{(2)}_{d,\mathrm{SDOF}}$ are the two SDOF impedances composing the DDOF equivalent target impedance $Z_{d,\mathrm{DDOF}}$. In this case, we can define the target frequency, mass and resistance coefficients for both the first ($f_{d,1}$, $\mu_{M,1}$, $r_{d,1}$) and second ($f_{d,2}$, $\mu_{M,2}$, $r_{d,2}$) degree of freedom of $Z_{d,\mathrm{DDOF}}$. We highlight that the DDOF equivalent behaviour is achieved on each ER, by the same controller transfer function of Eq. (2b), by simply replacing Z_d with $Z_{d,\mathrm{DDOF}}$.

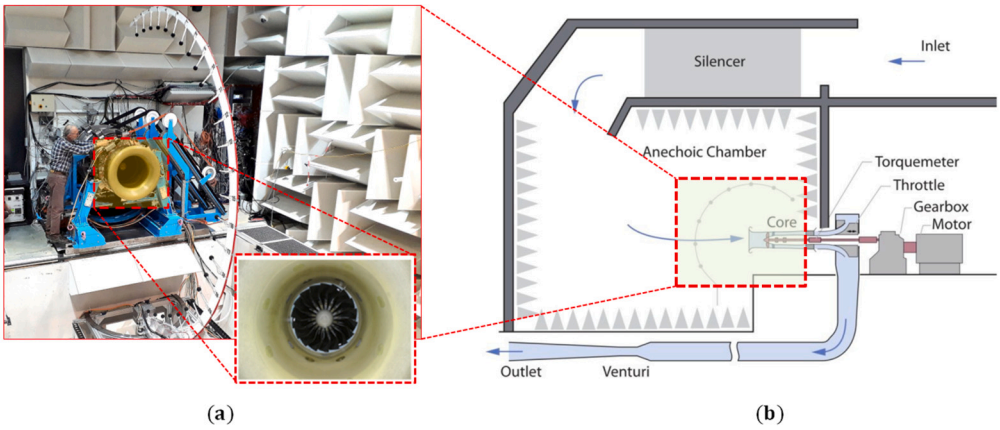

Fig. 2. 2D sketch of the entire test-rig **(b)**, with photo of the final stage of the turbofan **(a)** without turbulence screen and with zoom on the inside view in case of no liner (rigid reference).

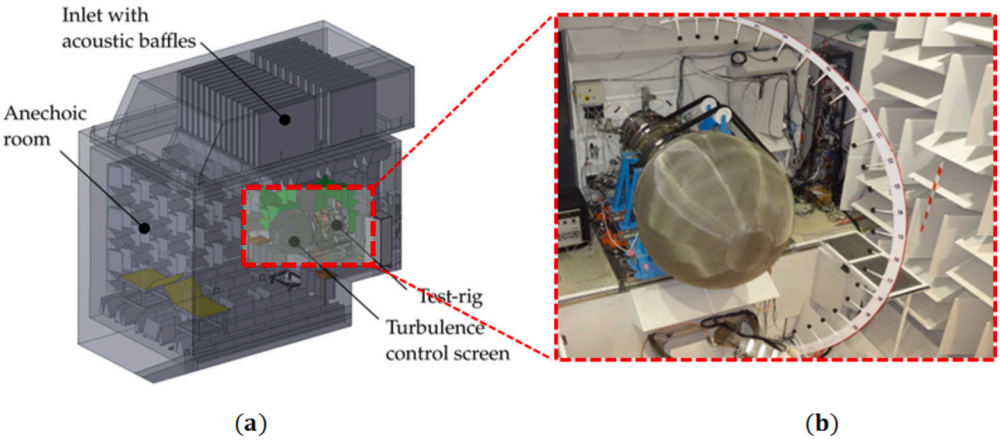

Fig. 3. 3D sketch of the entire test-rig **(a)**, with photo of the final stage of the turbofan **(b)** with turbulence screen.

2.2. Experimental setup

The ECL-B3 test-rig is located at the Laboratory of Fluid Mechanics and Acoustics (LMFA) of the Ecole Centrale de Lyon, in France. Part of the PHARE ANR-EquipEx program, the test-rig was designed in a close collaboration with Safran Aircraft Engines to perform multi-physics academic studies including aerodynamics, aeroelasticity, and aeroacoustics of UHBR turbofan engines at a 1:3 scale. The test-rig is located inside an anechoic chamber, as shown in Fig. 2. The rotational speed, up to 16 000 rotations per minute, is provided by a 3 MW electrical engine, and the internal diameter of the nacelle is $D = 50$ cm. The air flow, up to about 40 kg.s^{-1}, generated by the turbofan, passes through acoustic baffles on the roof of the building. The mass-flow rate is controlled, independently from the rotational speed, using a throttle system, and measured using a 20 m long Venturi tube, as shown in Fig. 2b. A turbulence control screen, made with honeycombs and wiremesh, is used to minimize the turbulence intensity ingested by the test-rig, as illustrated in Fig. 3.

Recently, interest was focused on the characterization of UHBR industrial turbofans, regarding acoustic aspects [57], modal decomposition [58], and aerodynamic instabilities [59]. Current and future test campaigns are dedicated to the realization of an academic open test-case [60–62].

The EL is applied in the inlet of the nacelle, as pictured in Figs. 4b and 5. Two rings of 28 ERs compose the EL, for a total lined segment length of 2×5 cm, meaning a ratio $L/D = 0.2$. Given the thickness of each ER, the thickness-to-diameter ratio is $d/D = 0.1$. Figs. 4b and 5 also show how the nacelle inlet has been modified in order to accommodate the EL. The frontal photo of Fig. 4a shows a pressure-balancing hole on the front face of the ER (close to the microphone B), needed in order to minimize the gap of static pressure between the nacelle interior traversed by air-flow, and the back-cavity of the ER, which might damage the membrane or affect its mobility. Notice that the EL is also protected from the air-flow, by a perforated plate and a wiremesh applied on top, as showed in Fig. 5. The main scope of the perforated plate and wiremesh is, indeed, to separate, to a reasonable extent, the aerodynamic field in the nacelle from the acoustic field applied on the ERs, therefore protecting the ERs' electromechanical components. Previous experimental campaigns with air-flows of Mach up to 0.3 [39] and 0.5 [48] have assured the correct performance of the ERs under significant air-flow conditions. Future investigations will be devoted to optimize the entire EL including perforated plate and wiremesh, while also taking into account a quantitative estimation of the impact of the pressure-balancing hole upon the overall behaviour.

2.3. Test conditions and performance indicators

In this section, we present the test conditions and the performance indicators employed to assess the EL performances. The analysis of the experimental results is provided in Section 3 with the following discussion in Section 4.

Fig. 6 shows the locations of the microphones employed for the assessment of the EL performances. The EL is located at the inlet of the nacelle, as showed in Fig. 6. Table 1 summarizes all the different test conditions employed in the experimental campaign, and the corresponding indicators to assess the EL performances. As the Power-Spectral-Density (PSD) spectra are not disclosable for confidential reasons, the sound pressure measurements upon the far-field microphone antenna are pre-

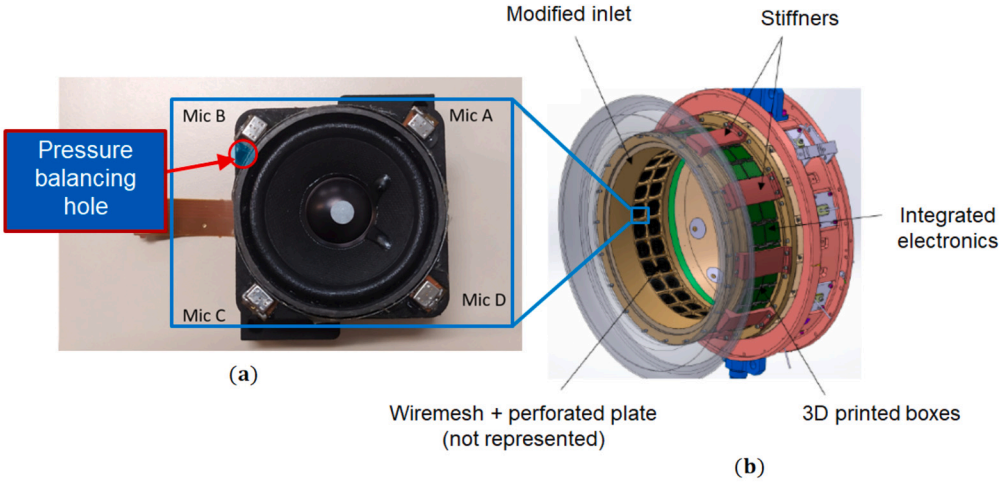

Fig. 4. ER photo **(a)** and sketch of the nacelle inlet without front wiremesh and perforated plate **(b)**.

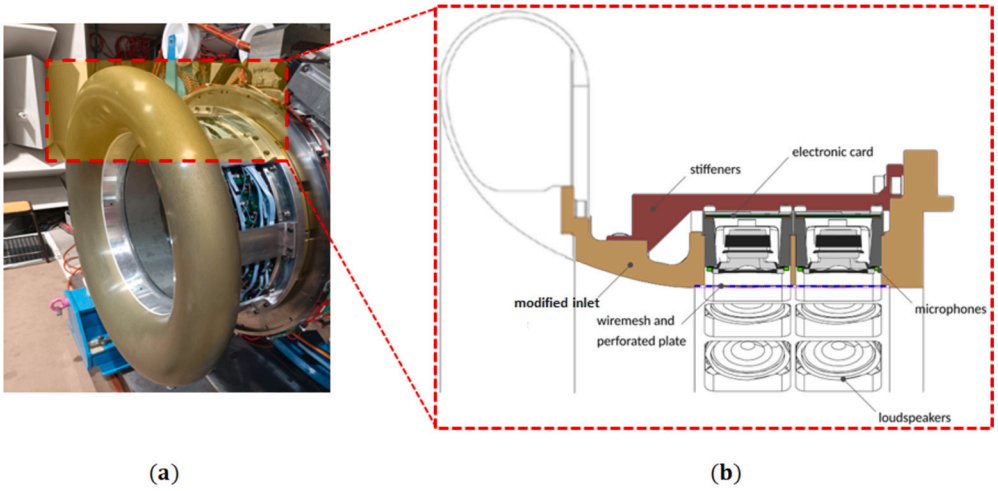

Fig. 5. Photo of the nacelle inlet with the EL covered by a wiremesh **(a)**, and sketch of the corresponding section **(b)**.

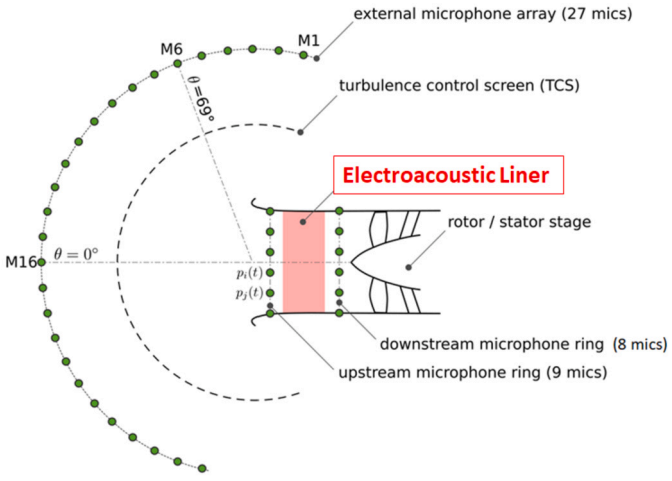

Fig. 6. Microphone arrays for the evaluation of the EL performances: external antenna with 27 microphones, in-duct upstream and downstream rings of 9 and 8 microphones, respectively.

sented in terms of Insertion Loss (IL) relative to the rigid reference. The rigid reference corresponds to the nacelle inlet without acoustic treatment, and is showed in the zoomed picture of the nacelle interior view in Fig. 2a. The IL directivity over a quarter of the circumference surrounding the nacelle inlet, is presented in terms of both tonal (IL_{tonal}) and broadband (IL_{broad}) components. In particular, the IL_{tonal} directivity is evaluated at the target frequency f_d of the EL, while the IL_{broad} directivity is evaluated at the Third-Octave-Band (TOB) containing f_d. Moreover, for IL_{total} (the IL of the total signal, comprising both tonal and broadband components) and IL_{broad}, we provide also the frequency spectra (in terms of TOBs), relative to the measurement of the microphone placed at a radiation angle $\theta = 69°$. The definitions of IL_{total}, IL_{tonal} and IL_{broad} are provided in Appendix A, along with the strategy employed to separate the tonal and broadband components, following [63]. Notice that, the definition of IL_{tonal} requires the evaluation of the *Average Band Power* (ABP) in the narrowest bandwidth surrounding the tone peak, given in Eq. (A.1) and (A.2) of Appendix A.

The far-field ILs are evaluated only upon the antenna microphones placed in the arc $\theta \in [0, 90°]$. This choice is due to measurement noise observed upon some microphones placed below the longitudinal axis of the nacelle, likely because of the proximity to the ground. Nevertheless, evaluating the liner performances on only a half of the radiation space outside the nacelle inlet, complies with some references [64,65], and is a reasonable laboratory choice, in the perspective of reducing aircraft noise radiation towards the earth, hence only towards half of the radiation space.

In case of $0.3N_n$, far field radiation performances are accompanied by the azimuthal mode amplitudes evaluated at two sections upstream and downstream the EL, accommodating 9 and 8 microphones respec-

Table 1
Test conditions and corresponding indicators employed for the assessment of the EL performances.

Test Conditions			Performance Indicators				
Engine Speed	f_d	M_∞	Azimuthal mode amplitudes	Far-field directivity of IL_{tonal} at f_d	Far-field directivity of IL_{broad} at TOB(f_d)	Spectra of IL_{total} at 69° microphone	Spectra of IL_{broad} at 69° microphone
$0.3N_n$	BPF	0.13	Yes	Yes	Yes	Yes	Yes
$0.4N_n$	BPF	0.18	NO	Yes	Yes	Yes	Yes
N_n	3 EO	0.56	NO	Yes	Yes	Yes	Yes
N_n	4 EO	0.56	NO	Yes	Yes	Yes	Yes
N_n	5 EO	0.56	NO	Yes	Yes	Yes	Yes

tively (see Fig. 6). According to the Shannon-Nyquist sampling theorem, these microphone arrays are sufficient to detect azimuthal modes up to the azimuthal order $m = \pm 4$. These modes dominate the acoustic propagation in the frequency range interested by the BPF at $0.3N_n$ engine speed. At higher regimes, more azimuthal modes become propagative and, therefore, significant for far-field radiation. Hence, only for the $0.3N_n$ regime, the azimuthal mode decomposition of the tonal signal at the BPF is provided in Section 3.1.1, along with the computational steps to obtain the azimuthal mode amplitudes. Notice that, in the plots of the azimuthal mode amplitudes (Fig. 8), the rigid-reference case is replaced by the Control-Off case, where no control is applied on the ERs. This choice is due to the fact that the modal amplitudes of the rigid-reference are protected by confidentiality. Nevertheless, since the BPF at $0.3N_n$ is sufficiently far from the resonance f_0 of the ERs in Control-Off, the impact of the EL in Control-Off is supposed to be very much reduced with respect to the Control-On configurations, where $f_d = \text{BPF}$.

3. Data analysis

After having outlined our EL technology and the test-rig (in Sections 2.1 and 2.2 respectively), we can proceed to the discussion of the experimental results at the test-conditions described in Section 2.3, by analysing the performance indicators.

3.1. Performances at 30% of nominal engine speed

In this section, the performances at $0.3N_n$ regime are reported, when the Mach number is about 0.13 in the nacelle inlet.

3.1.1. Azimuthal modes

The full duct mode decomposition formulation in a cylindrical acoustic waveguide with a uniform mean flow, is reported in Appendix B. Here, we conduct a so-called *azimuthal-only decomposition* [58], which starts by rewriting the modal decomposition of Eq. (B.9) as:

$$p_0(\omega, x, r, \phi) = \sum_{m=-\infty}^{\infty} C_m(x, r, \omega)\, e^{-\mathrm{j}m\phi}, \tag{7}$$

where $p_0(\omega, x, r, \phi)$ is the sound pressure frequency response at a point of cylindrical coordinates (x, r, ϕ) showed in Fig. 7, m is the azimuthal index of spinning modes, and C_m is the azimuthal mode amplitude, given by:

$$C_m(x, r, \omega) = \left[A^+_{m,n} e^{-\mathrm{j}k^+_{x_{(m,n)}} x} + A^-_{m,n} e^{-\mathrm{j}k^-_{x_{(m,n)}} x} \right] J_m(k_{r_{m,n}} r). \tag{8}$$

In Eq. (8), $A^+_{m,n}$ and $A^-_{m,n}$ are the modal participation factors of mode (m, n) propagating upstream and downstream respectively, relative to the corresponding wavenumbers $k^+_{x_{(m,n)}}$ and $k^-_{x_{(m,n)}}$, and the indexes $n = 1, 2\ldots$ are relative to the radial variation of the acoustic mode. Notice that, in $C_m(x, r, \omega)$, both upstream and downstream propagative contributions are included.

Eq. (8) can be written at each microphone azimuthal position ($r = R$, $\phi = \phi_i$), for $i = 1$ to N_ϕ, with N_ϕ the total number of microphones at a fixed section $x = x_0$, obtaining the matrix form:

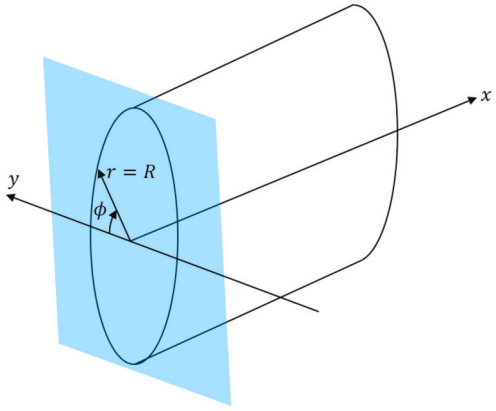

Fig. 7. Drawing of the cylindrical coordinates (x, r, ϕ), with r evaluated at the maximum radius R of the cross-section.

$$\mathbf{p}(\omega) = \mathbf{E} \cdot \mathbf{c}(\omega), \tag{9}$$

where $\mathbf{p}$ (size $[N_\phi \times 1]$) is the vector of complex pressures at each microphone azimuthal angle ϕ_i, $\mathbf{E}$ (size $[N_\phi \times N_m]$, with N_m the number of azimuthal modes of interest) is the matrix composed by the complex exponentials $e^{-\mathrm{j}m\phi_i}$, and $\mathbf{c}$ (size $[N_m \times 1]$) is the vector of azimuthal mode amplitudes C_m. Now, let us define the cross-power-spectral-density (CPSD) matrix $\mathbf{S_{pp}} \triangleq \mathbb{E}\{\mathbf{pp}^*\}$, where the superscript * denotes the conjugate transpose and the operator $\mathbb{E}$ stands for the expected value over a number of snapshots, as obtained by segmenting the time signals into short-time blocks, then Fourier transforming [58]. Replacing Eq. (9) in the definition of $\mathbf{S_{pp}}$, we get:

$$\mathbf{S_{pp}}(\omega) = \mathbb{E}\{\mathbf{p}(\omega)\mathbf{p}^*(\omega)\} = \mathbf{E}\, \mathbf{S_{cc}}(\omega)\, \mathbf{E}^*, \tag{10}$$

where $\mathbf{S_{cc}} = \mathbb{E}\{\mathbf{cc}^*\}$ is the modal CPSD matrix. So, from Eq. (10):

$$\mathbf{S_{cc}}(\omega) = \mathbf{E}^\dagger\, \mathbf{S_{pp}}(\omega)\, (\mathbf{E}^*)^\dagger, \tag{11}$$

where the superscript † represents the pseudo-inverse. Hence, the PSD of the azimuthal mode amplitude $C_m(\omega)$ are the diagonal terms of matrix $\mathbf{S_{cc}}(\omega)$ [58]. The maximum m index of detectable azimuthal modes is given by the Shannon-Nyquist sampling theorem, according to which the azimuthal sensor spacing should be less than or equal to half the maximum azimuthal wavelength λ_m of interest. The azimuthal spacing is $\Delta\phi = \phi_{i+1} - \phi_i = 2\pi/9$ for the upstream ring of microphones, and $2\pi/8$ for the downstream ring of microphones, while the azimuthal wavelength is $\lambda_m = 2\pi/m$. Therefore, the maximum detectable azimuthal mode index is $m = \pm 4$. From the wavenumber solution along the longitudinal direction x of a cylindrical duct with uniform flow, given by Eq. (B.8), we can easily obtain the expression of the cut-on frequency for the generic mode with radial index n and azimuthal index m:

$$f_{m,n} = \frac{c_0}{2\pi} k_{r_{(m,n)}} \sqrt{1 - M_\infty^2}. \tag{12}$$

In Eq. (12), c_0 is the sound speed, M_∞ the Mach number of the uniform flow, and $k_{r_{(m,n)}}$ the n^{th} eigenvalue of the Bessel function eigen-problem

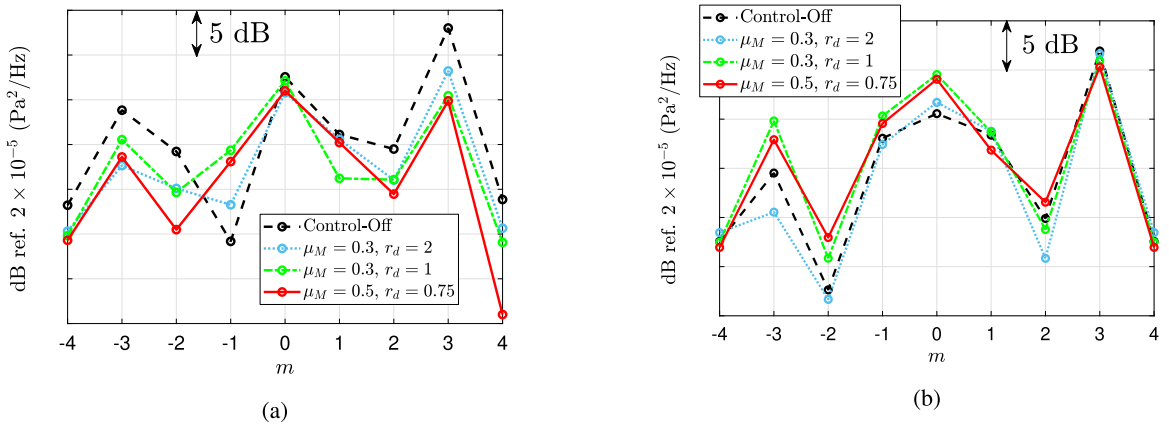

Fig. 8. Azimuthal mode amplitudes relative to the tonal component at the BPF of $0.3N_n$ on the upstream **(a)** and downstream **(b)** sections, respectively. The EL is tested in Control-Off and with various target SDOF impedances tuned at $f_d = \text{BPF}$.

$J'_m(k_{r_{(m,n)}}r)|_{r=R} = 0$, with $R = D/2 = 0.025$ m. For the mean-flow Mach number involved at $0.3N_n$, the first azimuthal mode with $m = \pm5$ is the mode $(m,n) = (\pm5, 1)$, which has a cut-on frequency at about 1390 Hz. As at $0.3N_n$, the BPF is placed well below such frequency, in this regime the acoustic propagation in the waveguide can be described by modes up to $m = \pm4$. Rigorously, as the EL is very close to the inlet termination, also evanescent modes contribute to the far-field propagation. Nevertheless, since the application of advanced signal processing techniques [58,66] is out of the scope of the present paper, a qualitative analysis can be conducted to check a possible correlation between detectable azimuthal mode amplitudes up to $m = \pm4$, and far-field radiation.

In Fig. 8a and 8b, the azimuthal mode amplitudes relative to the tonal component at the BPF of $0.3N_n$ on the upstream and downstream sections, respectively, are plotted. The EL is tested in Control-Off and with various target SDOF impedances tuned at $f_d = \text{BPF}$. The impact of the EL in Control-Off, on the modal propagation, can be qualitatively checked by the difference between upstream (Fig. 8a) and downstream (Fig. 8b) modal distribution. As this difference is appreciable, this means that the Control-Off differs from the rigid reference, as in the rigid case the difference between upstream and downstream modal content would be zero. Nevertheless, though the Control-Off cannot be assimilated with the rigid reference, it is still an useful benchmark to estimate the effect of the application of the control, as f_0 is sufficiently far from $f_d = \text{BPF}$. Moreover, since in the present work we are not interested in the acoustic energy reflected downstream, but we aim at mitigating the upstream noise transmission and the consequent radiation, our attention is focused here on the modal amplitudes at the upstream section and their possible correlation with far-field measurements. We should also keep in mind that the extracted modal amplitudes C_m, include both upstream and downstream propagating modes (see Eq. (8)). Nevertheless, supposing that the inward reflection from the inlet termination back inside the nacelle is not significantly affected by the EL, we can assume that the attenuation of modal amplitudes C_m achieved by our EL on the upstream section, is mostly representative of upstream noise transmission mitigation.

Fig. 8a shows that the highest energy content of the Control-Off (our benchmark) is concentrated on modes $m = 0$ and $m = \pm3$. In particular, the amplitude of mode $m = 3$ overcomes of more than 5 dB the amplitude of mode $m = 0$, and of more than 9 dB the amplitude of mode $m = -3$. The dominance of modes $m = \pm3$ with respect to the other modes with $m \neq 0$ is explained by the fact that the cut-on frequency of modes $m = \pm3$ is only slightly below the BPF at $0.3N_n$, and is the closest to the BPF compared to the other cut-on frequencies of azimuthal modes up to $m = \pm4$ [67]. Then, the prevalence of $m = 3$ with respect to $m = -3$ is explained by the corotation of mode $m = 3$ with the fan [67]. The higher energy content of a spinning mode $m = 3$ with respect to plane waves ($m = 0$) is also explained by the rotating nature of the noise source [67].

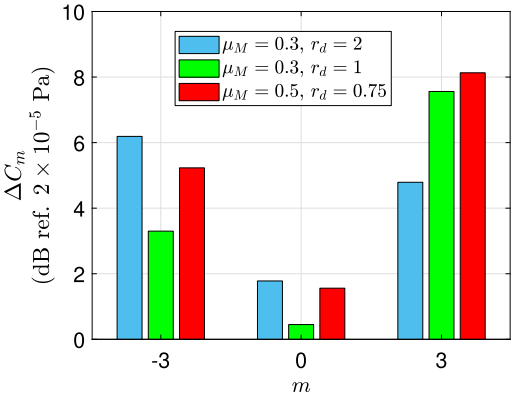

Fig. 9. Drawing of the cylindrical coordinates (x, r, ϕ), with r evaluated at the maximum radius R of the cross-section.

Looking at the most excited mode $m = 3$, the solid red curve corresponding to the highest quality factor (with $\mu_M = 0.5$ and $r_d = 0.75$, hence $Q = 0.94\sqrt{\mu_K}Q_0$), provides the largest attenuation of about 8.2 dB with respect to the Control-Off reference. Reducing the quality factor to $Q = 0.55\sqrt{\mu_K}Q_0$ (dashed-dot green curve) and $Q = 0.27\sqrt{\mu_K}Q_0$ (dotted blue curve), progressively reduces the $m = 3$ modal attenuation to respectively, to 7.5 and 5 dB. Mode $m = -3$ also presents good attenuation (about 5 dB with respect to the Control-Off) in case of $\mu_M = 0.5$ and $r_d = 0.75$, only slightly improved in case of $\mu_M = 0.3$ and $r_d = 2$. At $m = 0$, instead, all control configurations have very low impact at the upstream section, of maximum 1.8 dB. The impact of the control upon the principal azimuthal modes ($m = -3$, 0 and 3) at the BPF, is reported in Fig. 9 in terms of:

$$\Delta C_m = C_{m,\text{off}} - C_{m,\text{on}}, \tag{13}$$

where $C_{m,\text{off}}$ are the azimuthal mode amplitudes in the Control-Off reference case, and $C_{m,\text{on}}$ are the modal amplitudes when the control is applied. From Fig. 9, it is evident that each control configuration presents highest impact on mode $m = 3$, except for $\mu_M = 0.3$ and $r_d = 1$. In this latter control case, $\Delta C_{-3} = 6.2$ is higher than $\Delta C_3 = 4.8$. Nevertheless, as the Control-Off reference presents an azimuthal mode amplitude which is 9 dB higher than at mode $m = -3$ (see Fig. 8a), the attenuation of mode $m = 3$ is still the most significant in terms of IL.

To resume, mode $m = 3$ presents the highest amplitude in both the Control-Off and rigid reference, and the application of the control is particularly significant on this mode. After mode $m = 3$, is mode $m = 0$ in terms of energy content of the Control-Off reference, nevertheless, the application of the control provides negligible attenuation on $m = 0$. Then, it is mode $m = -3$ in terms of importance, and the application

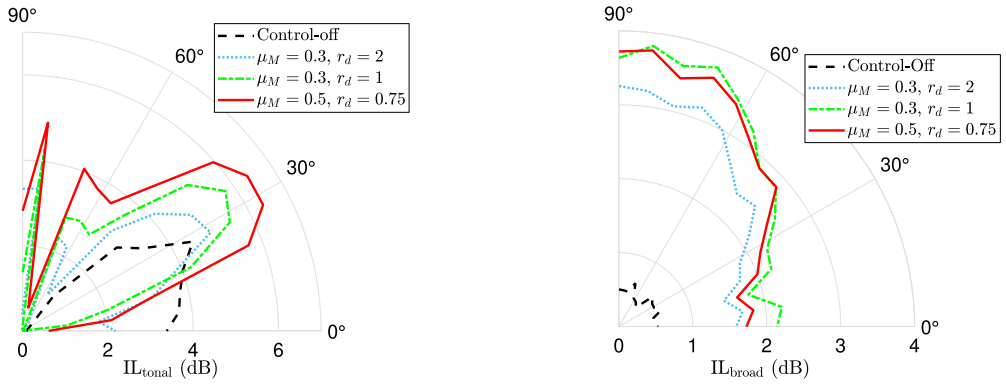

Fig. 10. Insertion Loss directivity of tonal component **(a)** (at the BPF) and broadband noise **(b)** (at the third-octave-band containing the BPF), in case of $0.3N_n$, with EL in Control-Off and with various target SDOF impedances tuned at $f_d = \text{BPF}$.

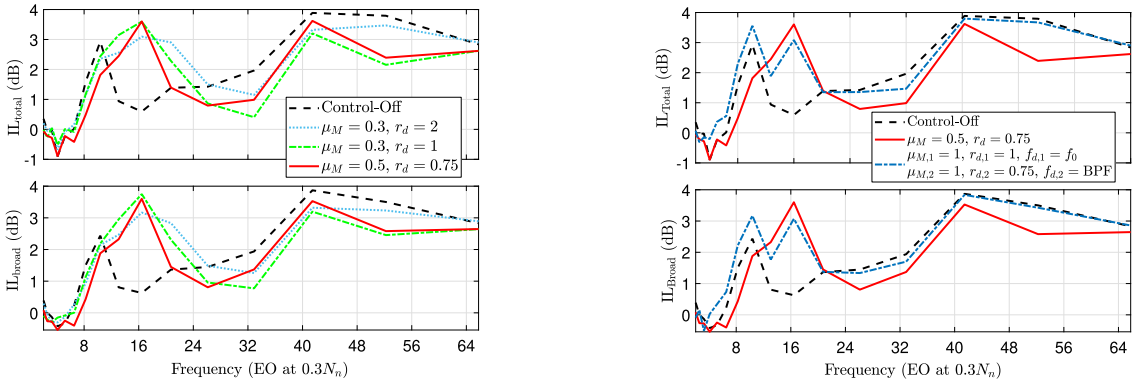

Fig. 11. IL of third-octave-band spectra of total and broadband noise at $0.3N_n$, on the microphone placed at 69° from the nacelle longitudinal axis, in case of Control-Off compared to SDOF target impedances with $f_d = \text{BPF}$ **(a)**, and to DDOF target impedance with $f_{d,1} = f_0$ and $f_{d,2} = \text{BPF}$ **(b)**.

of the control affects its amplitude in a comparable way with respect to mode $m = 3$. Nevertheless, as the Control-Off reference presents a 9 dB higher amplitude at mode $m = 3$, the attenuation of mode $m = -3$ due to the control has surely less impact on the overall sound pressure, compared to that on mode $m = 3$.

3.1.2. *Far-field radiation*

The far-field radiation over the microphones at $\theta \in [0°, 90°]$ surrounding the nacelle is analysed in this section, at the $0.3N_n$ regime. Fig. 10a shows the IL_{tonal} directivity at the BPF tone, in the same EL control cases as those of Fig. 8. Surprisingly, at $\theta = 0$, the IL_{tonal} in controlled configurations is lower than in case of Control-Off. Also, at $\theta = 76°$, a strong reduction of IL_{tonal} is displayed. Nevertheless, at all other radiation angles, the highest IL_{tonal} (up to 6 dB) is achieved by the solid red curve presenting the largest quality factor Q. This is in agreement with the results in terms of attenuation of the dominant azimuthal mode, showed in Fig. 8a. Notice also that, in the control-on cases, the highest IL_{tonal} is at values of $\theta \neq 0°$. This is in agreement with the fact that the control is mostly effective on azimuthal modes with $m \neq 0$, as showed in Fig. 8, which are related to radiation angles different from zero [11]. The three control configurations do not span all the possible impedance values, therefore we cannot draw a rule from these results. Nonetheless, based upon the available measurements, we can affirm a correlation between attenuation of the dominant mode $m = 3$ showed in Fig. 8a, far-field radiation, and quality factor of the EL target impedance. Besides, the complexity of the aeroacoustic test-rig requires a dedicated research towards the numerical optimization of the impedance which is out of the scope of the present paper. Here, our interest is to assess the potentialities of the EL in tuning at different engine speeds, and to extrapolate preliminary guidelines for the optimization of the target impedance parameters, based upon the measurements at disposal.

Fig. 10b shows the IL_{broad} directivity of the broadband noise at the third-octave-band containing the BPF. For the broadband noise, the IL_{broad} of the Control-Off case is very low as expected (because f_0 is relatively far from the BPF), and the highest IL is achieved by the target impedance with $\mu_M = 0.3$ and $r_d = 1$ at almost every radiation angles. We can speculate that such parameters present a compromise between efficient frequency bandwidth (enlarged thanks to lower μ_M), and low resistance which allows to increase the IL peak. This is in accordance with the tendencies observed for IL_{tonal}, and the role played by μ_M and r_d upon the target mobility [28].

Fig. 11a shows the IL of third-octave-band spectra of total and broadband noise, on the microphone placed at 69° from the nacelle longitudinal axis, with the same EL target impedances as Fig. 8 and 10. The IL values are reported on the third-octave-band centres, and the 69° radiation angle has been chosen as a representative case of non-axial radiations which mostly affect the noise pollution at the ground level. The frequency axis (the abscissae of Figs. 11a and 11b) are given in terms of EO = RPM/60, where 16 EO corresponds to the BPF as the rotor presents 16 blades. The Control-Off case presents a peak of IL at the third-octave-band centred between 10 EO and 11 EO (around f_0), but is not effective around the BPF. At the third-octave-band centred at about 16 EO (corresponding to the BPF), the IL_{broad} retrieves the results showed in the directivity of Fig. 10b, with $\mu_M = 0.3$ and $r_d = 1$ providing the best compromise between bandwidth and tonal peak. Between 20 EO and 32 EO, we see a reduction of IL for $\mu_M = 0.3$. This

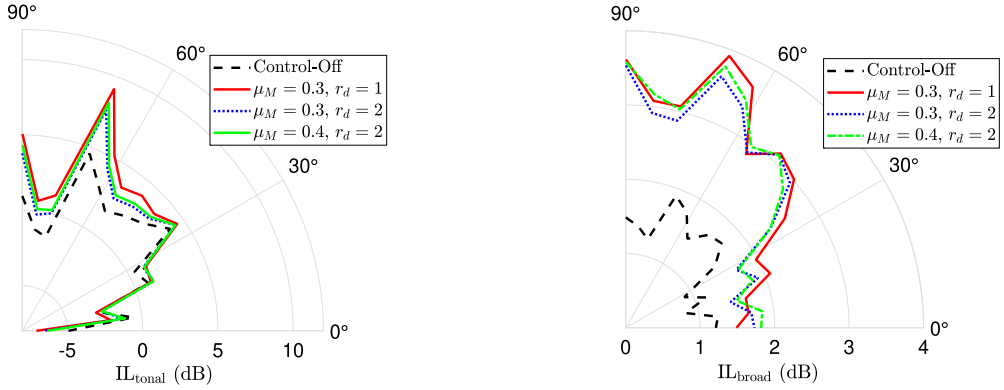

Fig. 12. Insertion Loss directivity of tonal component **(a)** (at the BPF) and broadband noise **(b)** (at the third-octave-band containing the BPF), in case of $0.4N_n$, with EL in Control-Off and with various SDOF target impedances tuned at $f_d = \mathrm{BPF}$.

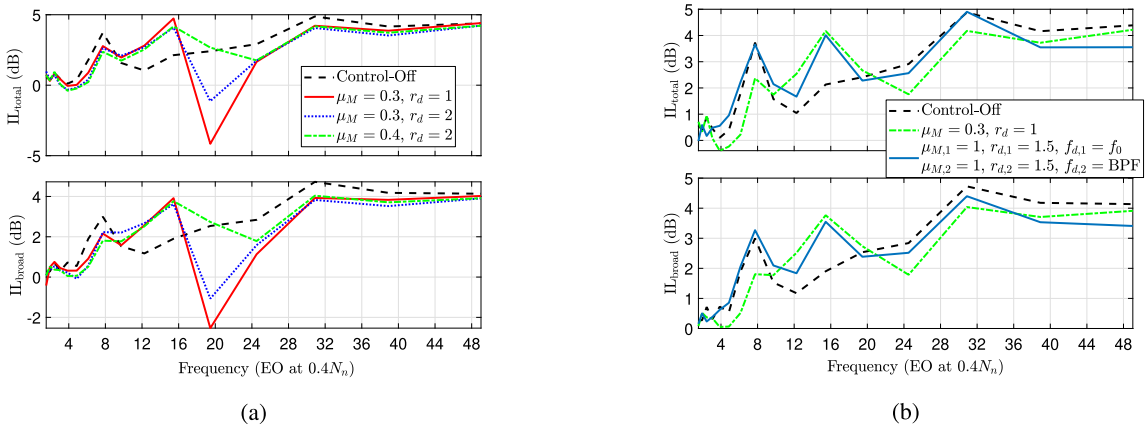

Fig. 13. IL of third-octave-band spectra of total and broadband noise at $0.4N_n$, on the microphone placed at 69° from the nacelle longitudinal axis, in case of Control-Off compared to SDOF target impedances with $f_d = \mathrm{BPF}$ **(a)**, and to DDOF target impedance with $f_{d,1} = f_0$ and $f_{d,2} = \mathrm{BPF}$.

is due to the physiological time delay in the digital control implementation, which endangers high-frequency acoustical passivity especially for lower mass-factors (ruling high-frequency responses of resonators), and resistances. Full details on the time-delay impact on acoustical passivity is provided in [28]. Increasing the resistance to $r_d = 2$, reduces the IL amplitudes in the BPF band, but enlarges the bandwidth outside of it and improves the high-frequency acoustical passivity, as expected from [28,38]. At higher frequencies (from about 32 EO), the IL augments due to the effect of the frontal wiremesh [68]. Another interesting result is obtained by targeting a DDOF impedance with resonance frequencies $f_{d,1} = f_0$ and $f_{d,2} = \mathrm{BPF}$, as showed in Fig. 11b. In that case, mass factors of both SDOF components are kept equal to 1 to assure sufficient acoustical passivity margin, because by increasing the mass coefficient high-frequencies will be less impacted by the digital control latency [28]. By targeting a DDOF impedance, good attenuation is achieved both at f_0 and at the BPF.

In this section, we demonstrated how the EL can be tuned to accomplish $\mathrm{IL_{tonal}}$ up to 6 dB and $\mathrm{IL_{broad}}$ up to 3.8 dB around the BPF at $0.3N_n$ regime. These performances are significant taking into account the low geometric ratios of the EL, and the low frequency of the BPF at $0.3N_n$.

3.2. Performances at 40% of nominal engine speed

At engine speed of $0.4N_n$, the Mach number is about 0.18 in the nacelle inlet, and the BPF is close to the cut-on frequency of mode $m = 5$. Hence, the azimuthal mode decomposition strategy, employing 8 and 9 fixed microphones (see Section 3.1.1), is not capable of fully describing the acoustic field in the nacelle intake. Therefore, the EL performances at $0.4N_n$ are evaluated only in terms of IL of far-field noise. Fig. 12a shows the $\mathrm{IL_{tonal}}$ directivity of the BPF tone for the EL in Control-Off and three other target impedances tuned at $f_d = \mathrm{BPF}$. First of all, we remark that for $\theta \leq 27.6°$, the $\mathrm{IL_{tonal}}$ is negative. This is likely due to a reshape of tonal directivity due to typical redistributions of modal contents [11]. As the non-axial radiation is the one mostly affecting the noise pollution at the ground, we shall focus on the attenuation along higher θ. The application of the control improves the $\mathrm{IL_{tonal}}$ with respect to the Control-Off case at every radiation angles $\theta > 27.6°$. For a fixed mass-factor $\mu_M = 0.3$, reducing the resistance r_d increases the tone attenuation at almost all radiation angles, reaching $\mathrm{IL_{tonal}}$ more than 9 dB at $\theta = 69°$, and staying above 3.5 dB for θ between 35° and 69°. Increasing r_d slightly reduces $\mathrm{IL_{tonal}}$ for $\theta \geq 35°$, and augmenting μ_M to 0.4 does not change much the $\mathrm{IL_{tonal}}$ directivity. Similar trends are featured in the $\mathrm{IL_{broad}}$ directivity at the third-octave-band containing the BPF, where the effect of the controller is much more evident compared to the Control-Off case. The $\mathrm{IL_{broad}}$ is between 3 and 3.9 dB for $\theta \geq 42°$, with slight variations among the three control configurations.

The $\mathrm{IL_{total}}$ and $\mathrm{IL_{broad}}$ spectra on the microphone at 69°, are showed in Fig. 13a. Apparently, a $\mu_M = 0.3$ is critical for acoustical passivity, as both $\mathrm{IL_{total}}$ and $\mathrm{IL_{broad}}$ present negative values at the third-octave-band centred at about 19 EO. Increasing r_d from 1 to 2 is not sufficient to restore acoustical passivity. By augmenting μ_M to 0.4, the acoustical passivity is restored, without significantly impacting neither IL spectra nor IL directivity. Fig. 13b demonstrates that the DDOF impedance with target frequencies $f_{d,1} = f_0$ (corresponding to about 8 EO, in case of $0.4N_n$) and $f_{d,2} = \mathrm{BPF}$ is capable of achieving significant noise attenuation around the BPF, meanwhile retaining good performances also at

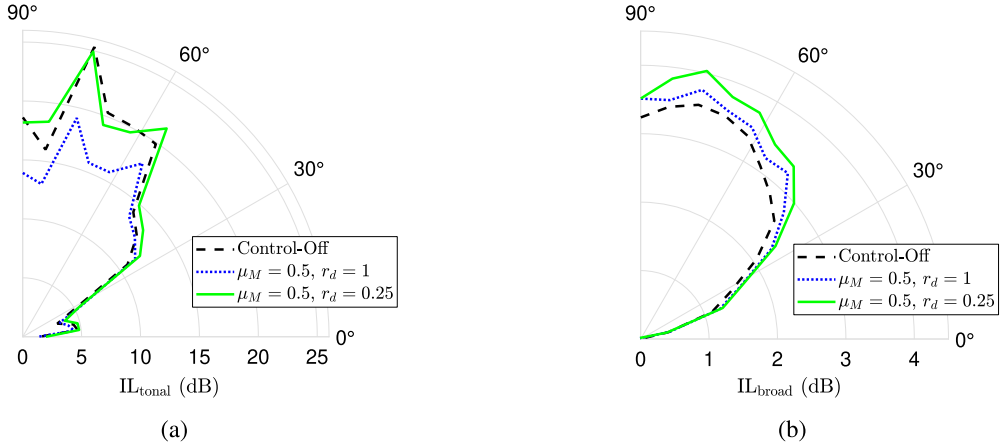

Fig. 14. Insertion Loss directivity of tonal component **(a)** at 3 EO, and broadband noise **(b)** at the third-octave-band containing 3 EO, in case of N_n regime, with EL in Control-Off and with various target SDOF impedances tuned at $f_d = 3$ EO.

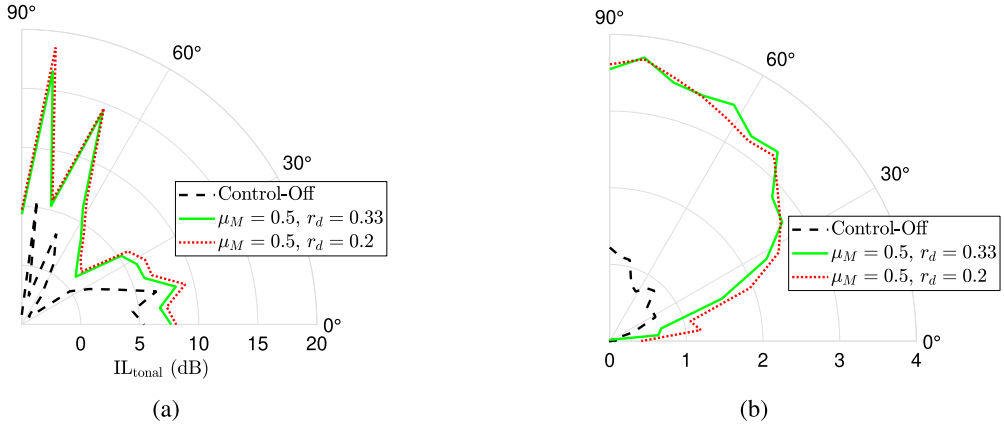

Fig. 15. Insertion Loss directivity of tonal component **(a)** at 4 EO, and broadband noise **(b)** at the third-octave-band containing 4 EO, in case of N_n regime, with EL in Control-Off and with various target SDOF impedances tuned at $f_d = 4$ EO.

much lower frequencies. As in case of $0.3N_n$, at frequencies above 2 kHz the wiremesh becomes effective.

In this section, we have demonstrated the capability of the EL to be tuned also at the BPF of a higher engine speed regime, achieving tonal noise reduction between 3.5 and 9 dB for radiation angles between 35° and 69°. Also, broadband noise attenuation up to 4 dB can be achieved in the BPF third-octave-band as well as at lower frequencies.

3.3. Performances at 100% of nominal engine speed

In this section, the EL is tested at the nominal engine speed N_n, with a Mach of about 0.56 in the nacelle inlet. In particular, the so-called "buzz-saw" noise [69], mentioned at the beginning of Section 3.3, is targeted. Such noise is composed by harmonics at EOs lower than the BPF, whose tonal peaks present comparable amplitudes than the one at the BPF. In particular, here we report the results of our EL targeting the frequencies relative to 3, 4 and 5 EO.

Fig. 14a shows the IL_{tonal} at 3 EO, in case of EL in Control-Off and with various target SDOF impedances tuned at $f_d = 3$ EO. We can observe that, for a fixed $\mu_M = 0.5$, reducing the resistance r_d leads to higher IL_{tonal}, once again correlating better tone attenuation with higher quality factors Q. Observe also that the Control-Off case presents approximately the same IL_{tonal} directivity as the SDOF target impedance with $\mu_M = 0.5$, $f_d = 3$ EO and $r_d = 0.25$. This should not surprise since we know that $f_0 \approx 3$ EO at N_n, therefore the EL in Control-Off is naturally tuned at 3 EO, and $\mu_K \approx \mu_M$ when control is applied to target 3 EO. Moreover, knowing that Control-Off means $\mu_M = 1$ and $R_d = R_0$, and that the natural resistance of the ERs is $R_0 \approx 0.5\rho_0 c_0$, this means a quality factor $Q \approx 2Q_0$ in Control-Off. When we apply the control with $\mu_M = 0.5$, $f_d = 3$ EO and $r_d = 0.25$, we retrieve once again $Q \approx 2Q_0$, which explains the similar IL_{tonal} directivity of the two configurations at 3 EO. For such quality factor, we get $IL_{tonal} > 10$ dB from $\theta = 34°$ to 90°, and $IL_{tonal} > 15$ dB from $\theta = 48°$ to 90°, overcoming 20 dB for $\theta \geq 55°$ with a peak of 25 dB at $\theta = 76°$.

Fig. 14b shows IL_{broad} at the third-octave-band containing 3 EO. We can notice that, for broadband noise, the application of the control allows to increase the IL_{broad} directivity thanks to a lower mass factor with respect to the Control-Off. Moreover, reducing r_d to 0.25 allows also to slightly augment the IL_{broad} directivity for $\theta \geq 35°$, reaching $IL_{broad} > 3$ dB for $\theta \geq 41.5°$ with a peak of 4 dB at $\theta = 76°$.

Fig. 17a shows the corresponding IL_{total} and IL_{broad} spectra in third-octave-bands, on the microphone placed at 69° from the nacelle longitudinal axis. We can notice that $\mu_M = 0.5$ allows to enlarge the bandwidth of both IL_{total} and IL_{broad} towards lower frequencies. In particular, we can realise that also the harmonic at 2 EO is attenuated by the EL: $IL_{total} \approx 4$ dB while $IL_{broad} = 3.5$ dB at the third-octave-band relative to 2 EO.

Fig. 15a shows the IL_{tonal} at 4 EO, in case of EL in Control-Off and with various target impedance parameters tuned at $f_d = 4$ EO. First of all, we notice that the Control-Off case presents negative values of IL_{tonal} for some radiation angles. This, once again, might be due to a redistribution of acoustic energy among duct modes, respect to the rigid

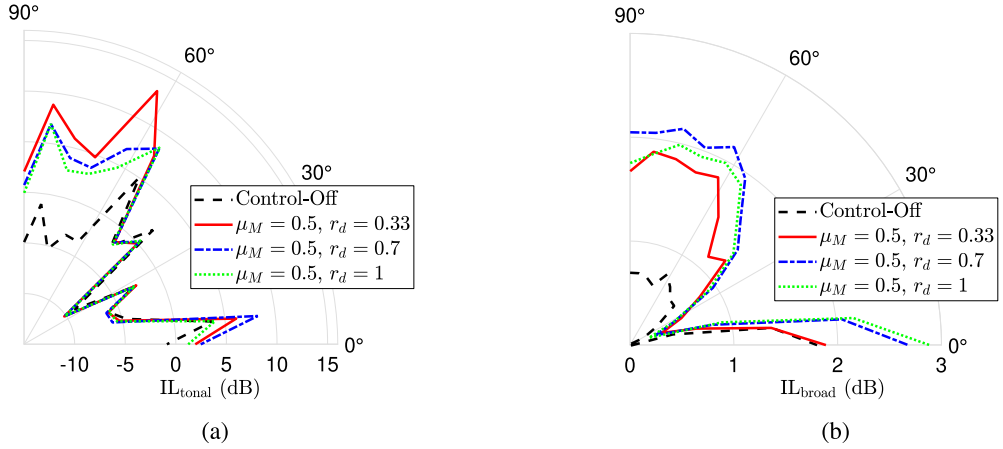

Fig. 16. Insertion Loss directivity of tonal component **(a)** at 5 EO, and broadband noise **(b)** at the third-octave-band containing 5 EO, in case of N_n regime, with EL in Control-Off and with various target SDOF impedances tuned at $f_d = 5$ EO.

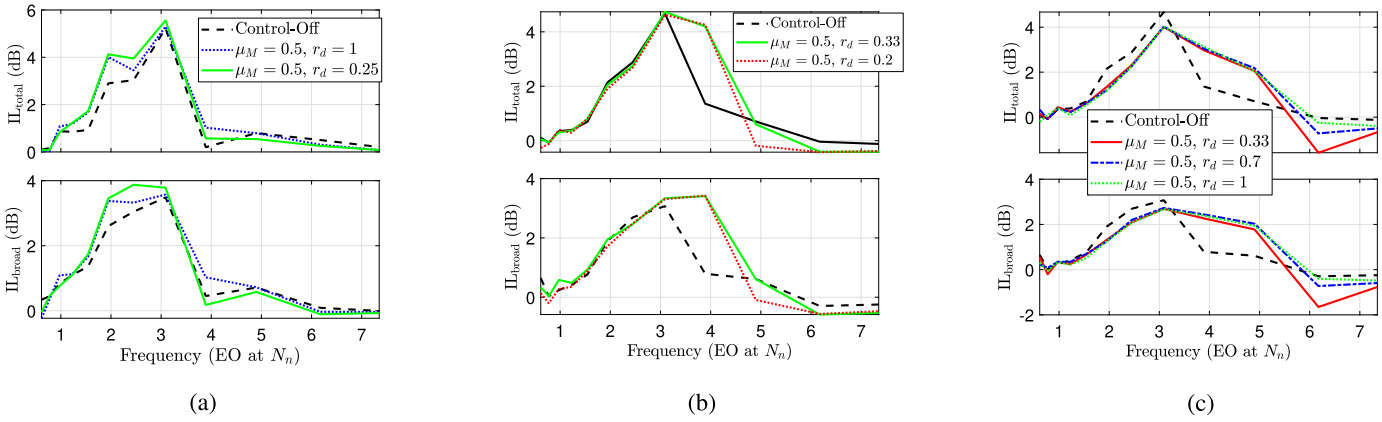

Fig. 17. IL of third-octave-band spectra of total and broadband noise at N_n, on the microphone placed at 69° from the nacelle longitudinal axis, for Control-Off and SDOF target impedances with $f_d = 3$ EO **(a)**, $f_d = 4$ EO **(b)** and $f_d = 5$ EO **(c)**.

reference, which results into a modification of the tonal directivity. By applying the control, an IL$_{tonal} > 5$ dB is featured except for radiation angles between 41° and 55°, reaching peaks of 14.6 dB and 18.6 dB at $\theta = 69°$ and 83°, respectively. Once again, increasing the quality factor (by reducing r_d) leads to slightly higher IL$_{tonal}$. Fig. 15b shows IL$_{broad}$ at the third-octave-band containing 4 EO. The IL$_{broad}$ of Control-Off is very low but positive, while the control implementation allows to reach IL$_{broad} > 3$ dB for $\theta \geq 48°$. Fig. 17b shows the corresponding IL$_{total}$ and IL$_{broad}$ spectra in third-octave-bands, on the microphone placed at 69° from the nacelle longitudinal axis. Observe that the EL is still effective on the 3 EO harmonic, because IL$_{total} > 4$ dB while IL$_{broad} \approx 3.3$ dB at 3 EO. Targeting $f_d = 4$ EO allows to enlarge the bandwidth from 3 to 4 EO, slightly improving the acoustical passivity at higher frequencies in case of larger r_d, as expected [28].

Fig. 16a shows the IL$_{tonal}$ at 5 EO, in case of EL in Control-Off and with various target SDOF impedances tuned at $f_d = 5$ EO. First of all, we notice that all configurations present negative values of IL$_{tonal}$ for θ between 5.5° and 41.5°. Apparently, the low-frequency harmonics excited by the buzz-saw noise at N_n present a directivity which is highly sensitive to the presence of the liner. Nevertheless, for $\theta \geq 55°$, IL$_{tonal}$ reaches significant values between 5 and 10 dB. In particular, for $\theta \geq 55°$, we remark the same tendency with the quality factor: reducing r_d leads to higher values of IL$_{tonal}$. In Fig. 15b, the corresponding IL$_{broad}$ at the third-octave-band centred at about 5 EO is plotted. Notice that the unexpected negative values of IL interest only the tonal noise, while IL$_{broad}$ is always positive, reaching more than 2 dB for $\theta > 55°$. We can observe that, when broadband noise is concerned, the highest quality factor does not bring the largest IL, but, usually, a compromise between bandwidth (larger for lower μ_M) and peak (higher for lower r_d) leads to the best IL$_{broad}$ at the targeted third-octave-band. Fig. 17b shows the corresponding IL$_{total}$ and IL$_{broad}$ spectra in third-octave-bands, on the microphone placed at 69° from the nacelle longitudinal axis. Comparing Fig. 17c, with Figs. 17a and 17b, we can notice the extension of the bandwidth relative to IL$_{total} \geq 2$ dB, from 2.5 to 5 EO. Nevertheless, for $r_d = 0.33$ and 0.7, acoustical passivity is endangered at 6 and 7 EO. By increasing r_d to 1, a good compromise is found between performances at f_d, and acoustical passivity at higher frequencies.

In this section, we have assessed the performances of the EL at nominal engine speed N_n, demonstrating the robustness of the EL technology against Mach number 0.56. Low-frequency harmonics of buzz-saw noise relative to 3, 4 and 5 EO have been targeted, demonstrating the capability of the EL to significantly attenuate the tones radiation at high θ, and enlarging the spectra of broadband noise attenuation. At 3 EO, the harmonic happens to fall close to f_0 and the highest IL$_{tonal}$ (up to 25 dB) is achieved. For higher EOs, the tone directivity is reshaped by the acoustic liner, with good IL$_{tonal}$ for $\theta > 55°$, and IL$_{tonal} < 0$ at some radiation angles. This unexpected behaviour is likely connected to a redistribution of acoustic energy among modes excited at the EO harmonics, but a modal analysis at this regime is out of the scope of the present paper. Nevertheless, such reshaping of directivity is still advantageous at high radiation angles, where high IL$_{tonal}$ is featured. Moreover, both total and broadband spectra show possible enlargement of IL from 3 EO up to 5 EO, with IL higher than 2 dB.

4. Discussion

In this section, we provide an overall discussion about the results at the three engine speed regimes reported in Section 3. At every regime, the directivity of IL_{tonal} seems to increase for higher quality factors of the target impedance, at almost all radiation angles $\theta \neq 0$. The extraction of in-duct azimuthal mode amplitudes at $0.3N_n$, in particular, has allowed to provide the physical correlation between the attenuation of the dominant mode, and the directivity pattern of IL_{tonal}. This result is interesting if compared with previous studies about optimal impedances from numerical simulations, such as [64], for which a corresponding finite optimal value of the quality factor should exist. This might indicate that the EL plus the wiremesh provide an equivalent quality factor which is always lower than the optimum one, in the studied control cases. Numerical simulations would allow to clarify about actual optimal impedances in our test-rig, and the role played by the quality factor, taking into account both the very low L/D ratio of our test-rig, and the peculiarity of a high amplitude tonal noise source.

Concerning the directivity, we have observed that IL_{tonal} can feature negative values at low radiation angles, both at $0.4N_n$ and, especially, at N_n. This might suggest a strong sensitivity of the directivity pattern upon the liner treatment. Nevertheless, as IL_{tonal} reaches positive and important values at higher radiation angles, the EL still results to be beneficial as long as the noise radiation towards the earth is concerned.

Then, the frequency spectra of IL_{total} and IL_{broad} on one microphone of the external antenna, have allowed to verify the specific roles played by the mass (μ_M) and resistance (r_d) coefficients, in terms of both acoustical passivity [28] and efficient bandwidth. When considering the attenuation in a broadband sense, over third-octave-bands, the lowest quality factor no longer leads to the highest performances. As expected by previous studies [28,39], a compromise between μ_M and r_d is needed in order to have good level of attenuation in a sufficiently large bandwidth, without jeopardizing acoustical passivity at higher frequencies. Finally, the implementation of a DDOF target impedance in the control transfer function, has allowed to target two resonant frequencies, therefore significantly enlarging the bandwidth of efficient attenuation.

Though not optimized, our EL has achieved very important attenuation levels when compared to the state-of-art with comparable geometric ratios (which, for our EL, are $L/D = 0.2$ and $d/D = 0.1$), though other parameters might influence the noise attenuation performances, such as the liner's position with respect to the noise sources.

5. Conclusions

In this paper, we have reported a detailed analysis of the first experimental campaign for the increase of Technology-Readiness-Level up to 3 of an innovative Electroacoustic Liner technology. The ECL-B3 (PHARE-2) turbofan rig has allowed to validate the Electroacoustic Liner concept into a representative turbofan facility, proving robustness when confronted to high Mach numbers (from 0.13 to 0.56) and tunability in attenuating noise at various Blade-Passing-Frequencies and low-frequency harmonics. At all engine speeds, lower quality factors of the target impedance feature higher far-field tonal noise attenuation. In particular, at 30% of nominal engine speed, the higher attenuation of tonal noise in far-field is accompanied by higher attenuation of the dominant in-duct azimuthal mode. Instead, regarding broadband noise, the best noise reduction is obtained at a compromise between high quality factor, and efficient bandwidth, as expected. At 30% of the nominal engine speed, tonal noise attenuation between 4 and 6.5 dB has been reached for radiation angles different than 0 and 76°, while broadband noise reduction more than 3.5 dB has been achieved around the BPF. At 40% of the nominal engine speed, tonal noise attenuation between 3 and 5 dB is reached at most radiation angles, while broadband noise reduction up to 4 dB is accomplished around the BPF. At 100% of the nominal engine speed, the Electroacoustic Liner has been tested against the low-frequency-harmonics of so-called "buzz-saw" noise [69]. Astonishing attenuation up to 25 dB is achieved for the third harmonic, as it falls close to the natural frequency of the Electroacoustic Resonators. At the fourth and fifth harmonics, instead, a significant reshaping of the tonal directivity happens, leading to sometimes negative Insertion Loss values at low radiation angles. Nevertheless, good tonal attenuation levels up to 15 dB are achieved at higher radiation angles which are the ones mostly impacting noise pollution at the ground level. In terms of total noise, the Electroacoustic Liner can achieve 2 to 5.6 dB of attenuation in the bandwidth between the second and fifth harmonics. These noise reduction levels are extremely significant, especially if compared with the state-of-art of experimental testing upon turbofans with comparable liner's length-over-diameter ratios. Moreover, the Electroacoustic Liner has proven to be able to enlarge its efficient bandwidth by synthesizing Double-Degree-Of-Freedom impedances. Next stages of this research will deal with numerical as well as experimental optimizations of the Electroacoustic Liner, taking into account the frontal wiremesh for the definition of optimal target impedances. In fact, the remote-control of the Electroacoustic Liner allows to scan all the desired target impedances even directly on the experimental test-bench, avoiding arduous numerical simulations.

This first experimental campaign opens the doors toward the implementation also of other type (possible generalized [38]) synthetic impedances, thanks to the Electroacoustic Resonator technology. Finally, lighter actuators are being developed in order to allow such programmable liners to fulfil the weight constraints.

CRediT authorship contribution statement

E. De Bono: Writing – review & editing, Writing – original draft, Visualization, Validation, Supervision, Software, Resources, Methodology, Investigation, Funding acquisition, Formal analysis, Data curation, Conceptualization. **E. Salze:** Supervision, Resources, Funding acquisition, Data curation. **M. Collet:** Visualization, Supervision, Resources, Project administration, Methodology, Funding acquisition, Conceptualization. **M. Gillet:** Software, Investigation. **M. Ouisse:** Supervision, Resources, Project administration, Methodology, Funding acquisition, Conceptualization. **M. Volery:** Visualization, Resources, Investigation. **H. Lissek:** Supervision, Resources, Project administration, Funding acquisition, Conceptualization. **J. Mardjono:** Visualization, Supervision, Software, Resources, Project administration, Funding acquisition.

Declaration of competing interest

The authors declare the following financial interests/personal relationships which may be considered as potential competing interests: Emanuele De Bono reports financial support was provided by Horizon 2020, grant agreement N∘ 821093. If there are other authors, they declare that they have no known competing financial interests or personal relationships that could have appeared to influence the work reported in this paper.

Acknowledgements

The SALUTE project has received funding from the Clean Sky 2 Joint Undertaking under the European Union's Horizon 2020 research and innovation programme under grant agreement N∘ 821093. This publication reflects only the author's view and the JU is not responsible for any use that may be made of the information it contains.

Authors are also particularly grateful to Benoit Paoletti, Cédric Desbois and Antonio Pereira for their precious help in setting up and conducting the experiments.

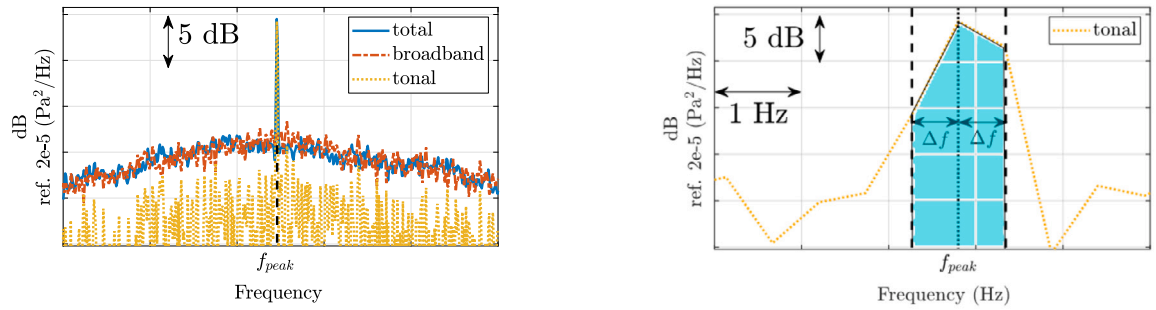

Fig. A.1. Example of separation of total, broadband and tonal components of the PSD around a BPF **(a)** obtained by the algorithm we have employed, and zoom around the BPF of the tonal component **(b)** for the definition of the frequency band used for computing the Average Band Power.

Appendix A. Separation of tonal and broadband noise components

The algorithm employed for the separation between broadband and tonal components follows the procedure proposed in [63]. The classical Time Synchronous Average method [70] mainly consists in separating the total time signal in blocks of length equal to the number of samples per revolution (NPR), then computing the arithmetic average of these blocks, and finally concatenating a sufficient number of averaged blocks in order to build an approximation of the tonal (deterministic) time signal. Indeed, the arithmetic average is meant to cancel out the broadband (random) component.

In [63], a *phase-adjustment* is proposed in order to compensate for phase-shifts randomly occurring between each block. Below, a summary of each step of the [63] algorithm is provided.

1. Separate the total time signal in blocks of length equal to NPR = $60 f_s/\mathrm{RPM}$, where f_s is the sampling frequency of the digital acquisition.
2. Label each segment as a or b in an alternating way, so that the total signal will be composed by the sequence of blocks $[a_1, b_1, a_2, b_2, a_3, b_3, ...]$
3. Take each couple consecutive blocks, say $a_i(t)$ and $b_i(t)$, and perform the cross-correlation to determine the *dominant phase shift* $\Delta\tau_i$ between them. The value of $\Delta\tau_i$ is given by the opposite of the abscissa corresponding to the maximum value of the cross-correlation between time signals $a_i(t)$ and $b_i(t)$. This means that if $b_i(t)$ leads $a_i(t)$, then $\Delta\tau_i < 0$, and viceversa.
4. Phase-adjust one of the blocks (either $a_i(t)$ or $b_i(t)$) according to the sign of $\Delta\tau_i$. For example, if $\Delta\tau_i$ is negative, it means that $b_i(t)$ leads $a_i(t)$ of a phase $|\Delta\tau_i|$, corresponding to a number of samples given by $|\Delta\tau_i| f_s$. Hence, the block $a_i(t)$ should be shifted forward of a number of samples equal to $|\Delta\tau_i| f_s$, i.e. $a_i^{\text{p.a.}}(t) = a_i(t - \Delta\tau_i f_s)$, where by $a_i^{\text{p.a.}}(t)$ we mean the corresponding *phase-adjusted* block. Viceversa, if $\Delta\tau_i$ is positive, it means that $a_i(t)$ leads $b_i(t)$, therefore the block $b_i(t)$ should be shifted forward, i.e. $b_i^{\text{p.a.}}(t) = b_i(t + \Delta\tau_i f_s)$.
5. Now, from each couple of phase-adjusted blocks, we can retrieve the broadband component as $w_i(t) = (a_i(t) - b_i(t))/\sqrt{2}$. This expression cancels out the common tone component, and assures that the mean-square value of $w_i(t)$ be equal to the mean square value of the random component of each block. Further details can be found in [63].
6. Hence, a *pseudo* broadband time signal can be reconstructed as $[w_1, w_2, w_3, ...]$.
7. Finally, the PSD of the broadband signal can be computed by classical Discrete-Fourier-Transform techniques. The PSD of the tonal component can be simply obtained by subtracting the PSD of the broadband component from the PSD of the total signal.

Fig. A.1a shows an example of total, broadband and tonal PSD spectra around a BPF, obtained by the above algorithm. Notice that no residual peak appears in the broadband spectrum.

However, because of the finite frequency resolution, here with a step $\Delta f = 0.5$ Hz, the actual level of the single tone can never be fully captured. Therefore, in order to provide experimental results in terms of IL, a scalar metric is needed to evaluate the actual acoustic energy at a tone. To do that, we make use of the average power over the narrowest frequency bandwidth around the peak, called *Average Band Power* (ABP), and defined as follows:

$$\mathrm{ABP}(f_{\text{tone}}) = \int_{f_{\text{peak}}-\Delta f}^{f_{\text{peak}}+\Delta f} \mathrm{PSD}(f)\,\mathrm{d}f, \tag{A.1}$$

where f is the frequency variable, f_{tone} is the actual frequency of the interested tone (the BPF for example), and f_{peak} is the frequency at the maximum value of the PSD closest to f_{tone} (see Fig. A.1b). Therefore, the IL for the tonal noise component at a specific f_{tone} can be defined as:

$$\mathrm{IL}_{\text{tonal}} = 10\log_{10}\Big(\mathrm{ABP}_{\text{Rigid}}(f_{\text{tone}})\Big) - 10\log_{10}\Big(\mathrm{ABP}_{\text{Lined}}(f_{\text{tone}})\Big), \tag{A.2}$$

where $\mathrm{ABP}_{\text{Rigid}}(f_{\text{tone}})$ and $\mathrm{ABP}_{\text{Lined}}(f_{\text{tone}})$ are the ABP at the interested f_{tone} in case of rigid and lined nacelle inlet, respectively.

For the total and broadband noise, instead, the third-octave PSD spectra are employed to compute the IL as:

$$\mathrm{IL}_{\text{total}} = 10\log_{10}\Big(\mathrm{PSD}^{\text{total}}_{\text{Rigid}}(\Delta f_{\text{TOB}})\Big) - 10\log_{10}\Big(\mathrm{PSD}^{\text{total}}_{\text{Lined}}(\Delta f_{\text{TOB}})\Big), \tag{A.3a}$$

$$\mathrm{IL}_{\text{broad}} = 10\log_{10}\Big(\mathrm{PSD}^{\text{broad}}_{\text{Rigid}}(\Delta f_{\text{TOB}})\Big) - 10\log_{10}\Big(\mathrm{PSD}^{\text{broad}}_{\text{Lined}}(\Delta f_{\text{TOB}})\Big), \tag{A.3b}$$

where $\mathrm{PSD}^{\text{total}}_{\text{Rigid}}(\Delta f_{\text{TOB}})$ and $\mathrm{PSD}^{\text{total}}_{\text{Rigid}}(\Delta f_{\text{TOB}})$ are the third-octave-band (TOB) spectra of total noise in case of rigid and lined nacelle inlet, while $\mathrm{PSD}^{\text{broad}}_{\text{Rigid}}(\Delta f_{\text{TOB}})$ and $\mathrm{PSD}^{\text{broad}}_{\text{Lined}}(\Delta f_{\text{TOB}})$ are the equivalent spectra relative to the broadband noise.

Appendix B. Duct mode decomposition in a cylindrical acoustic duct

Let us consider a uniform cylinder of radius R with x the longitudinal axis, and y and z defining the cross-section plane. In case of a uniform air-flow along x, the wave equation writes:

$$\frac{1}{c_0^2} D_t^2 p(x,y,z,t) = \nabla^2 p(x,y,z,t), \tag{B.1}$$

with c_0 the sound speed, p the acoustic pressure, ∇^2 the Laplacian operator, $D_t = \partial_t + V_x\partial_x$ the Lagrangian (also called *substantial* or *convective*) derivative, and V_x the air-flow (convection) speed. The Laplacian operator, in the cylindrical coordinates (r, ϕ, x) showed in Fig. 7, writes:

$$\nabla^2 = \partial_x^2 + \partial_r^2 + \frac{1}{r^2}\partial_\phi^2 + \frac{1}{r}\partial_r. \tag{B.2}$$

In the linear and stationary regime, the solution can be analysed in terms of its Fourier components written in the frequency domain:

$$\hat{p}(\omega, t, x, r, \phi) = p_0(\omega, x, r, \phi)e^{\mathrm{j}\omega t}. \tag{B.3}$$

Inserting Eq. (B.3) in the convected wave Eq. (B.1) written in polar coordinates, we get the so-called Helmholtz convected wave equation:

$$\left(-k_0^2 + 2M_\infty \mathrm{j}k_0\partial_x + M_\infty^2\partial_x^2\right)p_0 = \left(\partial_x^2 + \partial_r^2 + \frac{1}{r^2}\partial_\phi^2 + \frac{1}{r}\partial_r\right)p_0, \tag{B.4}$$

with $k_0 = \omega/c_0$ the wave number of plane waves in absence of flow, and $M_\infty = V_x/c_0$ the Mach number of the air-flow. A solution of the homogeneous Eq. (B.4) is given by separation of variables technique, as:

$$p_0(\omega, x, r, \phi) = P(r)\, e^{-\mathrm{j}m\phi}e^{-\mathrm{j}k_x x}. \tag{B.5}$$

By inserting Eq. (B.5) in Eq. (B.4), we get:

$$\left(\partial_r^2 + \frac{1}{r}\partial_r\right)P(r) = \left[-(k_0 - M_\infty k_x)^2 + k_x^2 + \frac{m^2}{r^2}\right]P(r), \tag{B.6}$$

which can be rewritten as:

$$\left(\partial_r^2 + \frac{1}{r}\partial_r\right)P(r) = \left[-k_{r_{(m,n)}}^2 + \frac{m^2}{r^2}\right]P(r), \tag{B.7}$$

with $k_{r_{(m,n)}}^2 = -(k_0 - M_\infty k_x)^2 + k_x^2$. Eq. (B.7) is an eigenvalue problem of the Bessel type, with eigenfunctions $P(r)$ and eigenvalues $k_{r_{(m,n)}}$ [36]. Eq. (B.7) must be accompanied by the boundary condition on the external radius $r = R$ of the cylindrical domain which, in case of hard walls, is the impenetrability condition on the rigid cylindrical boundary, i.e. $\partial_r p = d_r P(r) = 0$ [36]. By doing so, the solutions of Eq. (B.7), finite at the origin $r = 0$, are Bessel functions of the first kind and order m: $P(r) = P_{m,n}J_m(k_{r_{m,n}}r)$, where the eigenvalues $k_{r_{m,n}}$ are obtained from the known solutions of $J_m'(k_{r_{(m,n)}}r)|_{r=R} = 0$ [36].

Once $k_{r_{(m,n)}}$ is known, $k_{x_{(m,n)}}$ is obtained from:

$$k_{x_{(m,n)}} = \frac{k_0}{1 - M_\infty^2}\left(-M_\infty \pm \sqrt{1 - (1 - M_\infty^2)\frac{k_{r_{(m,n)}}^2}{k_0^2}}\right). \tag{B.8}$$

Eq. (B.8) gives the propagation characteristics along the longitudinal axis, i.e. its sense and velocity of propagation (given by the sign and amplitude of its real part) and its attenuation or amplification (given by the sign and amplitude of its corresponding imaginary part).

Now we can finally write the acoustic frequency-response, sufficiently far from discontinuities, in a cylindrical waveguide, as the sum on all the guided-modes excited by the sources:

$$p_0(\omega, x, r, \phi) = \sum_m \sum_n \left[A_{m,n}^+ e^{-\mathrm{j}k_{x_{(m,n)}}^+ x} + A_{m,n}^- e^{-\mathrm{j}k_{x_{(m,n)}}^- x}\right]J_m(k_{r_{m,n}}r)\, e^{-\mathrm{j}m\phi}, \tag{B.9}$$

where $A_{m,n}^+$ and $A_{m,n}^-$ are the modal participation factors of mode (m, n) propagating upstream and downstream respectively, relative to the corresponding wavenumbers $k_{x_{(m,n)}}^+$ and $k_{x_{(m,n)}}^-$. The indexes $n = 1, 2\ldots$ are relative to the radial variation of the acoustic mode ($n = 2$ means one circumferential nodal line), while $m = 0, \pm1, \pm2\ldots$ are relative to the azimuthal variation of the acoustic mode ($m = 1$ means one diametrical nodal line). Observe that the constant phase of the acoustic modes defined in Eq. (B.5) and (B.9) travels along the x axis, as well as along the azimuthal direction ϕ for $m \neq 0$. Those with $m \neq 0$ are called *spinning modes*, which are typically excited by ducted fans.

Appendix C. List of acronyms

- ABP: Average Band Power around the tone
- $\mathrm{ABP}_{\mathrm{Lined}}$: Average Band Power in the lined case
- $\mathrm{ABP}_{\mathrm{Rigid}}$: Average Band Power in the rigid case
- ADC: Analogue-Digital-Converter
- ANC: Active Noise Cancellation
- BPF: Blade-Passing-Frequency
- CPSD: Cross-Power-Spectral-Density
- DDOF: Double-Degree-Of-Freedom
- DSP: Digital-Signal-Processor
- EL: Electroacoustic Liner
- EO: Engine Order of the turbofan
- ER: Electroacoustic Resonator
- IIR: Infinite-Impulse-Response
- IL: Insertion Loss
- $\mathrm{IL}_{\mathrm{broad}}$: IL of the broad signal in third-octave bands
- $\mathrm{IL}_{\mathrm{total}}$: IL of the total signal in third-octave bands
- NPR: Number of samples per revolution of the fan
- PSD: Power-Spectral-Density
- $\mathrm{PSD}_{\mathrm{Lined}}^{\mathrm{broad}}$: PSD of the broad signal in the lined case
- $\mathrm{PSD}_{\mathrm{Lined}}^{\mathrm{total}}$: PSD of the total signal in the lined case
- $\mathrm{PSD}_{\mathrm{Rigid}}^{\mathrm{broad}}$: PSD of the broad signal in the rigid case
- $\mathrm{PSD}_{\mathrm{Rigid}}^{\mathrm{total}}$: PSD of the total signal in the rigid case
- PWL: Power Level
- SDOF: Single-Degree-Of-Freedom
- SPL: Sound Pressure Level
- TOB: Third-Octave-Band
- TRL: Technology-Readiness-Level
- UHBR: Ultra-High-Bypass-Ratio

Appendix D. List of symbols

- a_i, b_i: couple of consecutive blocks of the acquired signals, each of length equal to NPR
- $a_i^{\mathrm{p.a.}}$: phase-adjusted block a_i
- $b_i^{\mathrm{p.a.}}$: phase-adjusted block b_i
- $A_{m,n}^{\pm}$: Modal participation factor of mode (m,n) propagating downstream (+) or upstream (−)
- Bl: Force factor of the loudspeaker
- $\mathbf{c}$: vector of azimuthal mode amplitudes C_m
- c_0: speed of sound
- C_f: Capacitance of the compensation circuit in the Howland current pump
- C_m: Azimuthal mode amplitudes
- D: Nacelle internal diameter
- d: Liner thickness
- D_t: Lagrangian derivative $\partial_t + V_x\partial_x$
- $\mathbf{E}$: matrix composed by the complex exponentials $e^{\mathrm{j}m\Phi_i}$
- $\mathbb{E}$: expected value
- f_0: Resonance frequency of the loudspeaker in open circuit
- f_d: Desired resonance frequency of the ER desired acoustical impedance
- f_s: sampling frequency of the digital acquisition
- f_{peak}: frequency at the maximum value of the PSD closest to f_{tone}
- f_{tone}: frequency of the interested tone where to evaluate ABP
- H_{Loc}: Control transfer function
- $\tilde{i}$: Electrical current in the Laplace domain, in the loudspeaker coil
- j: Imaginary unit
- J_m: Bessel function of the first type and order m
- J_m': first derivative of the Bessel function of the first type and order m

- K_0: Acoustical stiffness of the loudspeaker in open circuit
- K_d: Desired acoustical stiffness of the ER desired acoustical impedance
- k_0: ω/c_0
- $k_{r_{m,n}}$: Radial wavenumber of mode (m,n)
- k_x: generic axial wavenumber in the ansatz of Eq. (B.5)
- $k^{\pm}_{x_{m,n}}$: Axial wavenumber of mode (m,n) propagating downstream (+) or upstream (−)
- L: Liner length
- M_0: Acoustical mass of the loudspeaker in open circuit
- M_∞: air-flow Mach number
- M_d: Desired acoustical mass of the ER desired acoustical impedance
- m: Azimuthal modal order
- n: Radial mode order
- N_Φ: Total number of microphones in the nacelle cross-section
- N_m: number of azimuthal modes of interest
- N_n: Nominal engine speed of the PHARE-2 turbofan
- $\bar{p}$: Sound pressure in the Laplace domain, on the loudspeaker membrane
- p_0: Sound pressure frequency response in the nacelle
- $\mathbf{p}$: vector of complex pressures at each microphone azimuthal angle
- Q: Quality-factor of the ER desired acoustical impedance
- Q_0: Quality-factor of the loudspeaker in open circuit
- R: Radius of the nacelle
- R_0: Acoustical resistance of the loudspeaker in open circuit
- R_d: Desired acoustical resistance of the ER desired acoustical impedance
- R_d: Resistance of the compensation circuit in the Howland current pump
- R_f: Feedback resistor in the Howland current pump
- R_i: Input resistor in the Howland current pump
- R_s: Current sense resistor in the Howland current pump
- r: Radial coordinate in the cylindrical nacelle
- r_d: Ratio $R_d/\rho_0 c_0$
- s: Laplace variable
- S_e: Effective surface area of the loudspeaker membrane
- $\mathbf{S_{cc}}$: CPSD matrix of the modal amplitudes
- $\mathbf{S_{pp}}$: CPSD matrix of the sound pressures
- $\bar{v}$: Acoustic velocity in the Laplace domain, on the loudspeaker membrane
- V_x: air-flow axial velocity
- w_i: broadband component of blocks a_i and b_i
- x: Axial coordinate in the cylindrical nacelle
- Z_0: Acoustical impedance of the loudspeaker in open circuit
- Z_d: Desired acoustical impedance of the ER
- $Z_{d,DDOF}$: Double-Degree-Of-Freedom desired acoustical impedance of the ER
- ∂_r: radial derivative
- ∂_Φ: azimuthal derivative
- ∂_x: x-derivative
- $\Delta\tau_i$: dominant phase shift between blocks a_i and b_i
- Δf_{TOB}: third-octave-band frequency range
- θ: Radiation angle from the turbofan
- μ_K: Ratio K_d/K_0
- μ_M: Ratio M_d/M_0
- ∇^2: Laplacian operator in cylindrical coordinates
- ρ_0: static air density
- Φ: Azimuthal coordinate in the cylindrical nacelle
- Φ_i: Azimuthal coordinate of the i-th microphone in the nacelle cross-section
- ω: Angular frequency

Data availability

The data that has been used is confidential.

References

[1] European Commission. Directorate-general for mobility and transport and directorate-general for research and innovation, flightpath 2050 – Europe's vision for aviation – maintaining global leadership and serving society's needs. Publications Office; 2011.
[2] De Bono E, Fernandes AD, Petrone G, Ouisse M, Teloli R. On the optimization of (generalized) impedance for acoustic liners. In: 34th ICAS (ICAS2024); 2024.
[3] Oh TS, Jeon W. Acoustic metaliners for sound insulation in a duct with little flow resistance. Appl Phys Lett 2022;120.
[4] Zhao J, Wu F, Ju Z-G, Hu M, Zhang X, Li D, et al. Neck-embedded acoustic meta-liner for the broadband sound-absorbing under the grazing flow with a wide speed range. J Phys D, Appl Phys 2022;56:45401.
[5] Catapane G, Petrone G, Robin O. Series and parallel coupling of 3D printed micro-perforated panels and coiled quarter wavelength tubes. J Acoust Soc Am 2023;154:3027–40.
[6] Wang Y, Qiu X, Du L, Jing X, Sun X. Investigation of broadband performance of periodic parallel-element liners with multi-layer acoustic septa. In: 30th AIAA/CEAS aeroacoustics conference (2024); 2024. p. 3300.
[7] Howerton BM, Kreitzman JR, Solano C. Extending acoustic liner bandwidth with simple embedded septa. In: 30th AIAA/CEAS aeroacoustics conference (2024); 2024. p. 3302.
[8] Choy YS, Huang L. Drum silencer with shallow cavity filled with helium. J Acoust Soc Am 2003;114:1477–86.
[9] Palani S, Subramanyam RR, Paruchuri C, Joseph P. Flexible membrane type nonlinear liner. In: 29th international congress of sound and vibration; 2023.
[10] Rice E. Acoustic liner optimum impedance for spinning modes with mode cut-off ratio as the design criterion. In: 3rd aeroacoustics conference; 1976. p. 516.
[11] Rice E, Heidmann M, Sofrin T. Modal propagation angles in a cylindrical duct with flow and their relation to sound radiation. In: 17th aerospace sciences meeting; 1979. p. 183.
[12] Sutliff DL. Advanced noise control fan: a 20-year retrospective of contributions to aeroacoustics research. Technical Report. 2019.
[13] Ma X, Su Z. Development of acoustic liner in aero engine: a review. Sci China, Technol Sci 2020:1–14.
[14] Sutliff DL, Nark DM, Jones MG, Schiller NH. Design and acoustic efficacy of a broadband liner for the inlet of the DGEN aero-propulsion research turbofan. In: 25th AIAA/CEAS aeroacoustics conference; 2019. p. 2582.
[15] Ingard U. Noise reduction analysis. Jones & Bartlett Publishers; 2009.
[16] Burdisso R, Smith J. Control of inlet noise from turbofan engines using Herschel-Quincke waveguides. In: 6th aeroacoustics conference and exhibit; 2000. p. 1994.
[17] Burdisso RA, Ng WF, Provenza A. Fan noise control using Herschel-Quincke resonators. Technical Report. 2003.
[18] Sijtsma P, van der Wal H. Modelling a spiralling type of non-locally reacting liner. In: 9th AIAA/CEAS aeroacoustics conference and exhibit; 2003. p. 3308.
[19] Maier R, Zillman J, Roure A, Winninger M, Enghardt L, Tapken U, et al. Active control of fan tone noise from aircraft engines. In: 7th AIAA/CEAS aeroacoustics conference and exhibit; 2001. p. 2220.
[20] Zillmann J, Tapken U. Tonal noise radiation from UHBR fan-active control of radiation characteristic. In: 15th AIAA/CEAS aeroacoustics conference (30th AIAA aeroacoustics conference); 2009. p. 3226.
[21] Yamasaki N, Tajima H. Active control of fan noise. J Therm Sci 2008;17:163–9.
[22] Olson HF, May EG. Electronic sound absorber. J Acoust Soc Am 1953;25:1130–6.
[23] Fleming AJ, Niederberger D, Moheimani SO, Morari M. Control of resonant acoustic sound fields by electrical shunting of a loudspeaker. IEEE Trans Control Syst Technol 2007;15:689–703.
[24] Furstoss M, Thenail D, Galland M. Surface impedance control for sound absorption: direct and hybrid passive/active strategies. J Sound Vib 1997;203:219–36.
[25] Leo DJ, Limpert DK. Self-sensing technique for active acoustic attenuation. In: Collection of technical papers - AIAA/ASME/ASCE/AHS/ASC structures, structural dynamics and materials conference, vol. 4. Reston, Virginia: American Institute of Aeronautics and Astronautics; 1999. p. 2603–10.
[26] Malléjac M, Volery M, Lissek H, Fleury R. Active control of electroacoustic resonators in the audible regime: control strategies and airborne applications. npj Acoust 2025;1:4.
[27] Rivet E, Karkar S, Lissek H. Broadband low-frequency electroacoustic absorbers through hybrid sensor-/shunt-based impedance control. IEEE Trans Control Syst Technol 2017;25:63–72.
[28] De Bono E, Collet M, Matten G, Karkar S, Lissek H, Ouisse M, et al. Effect of time delay on the impedance control of a pressure-based, current-driven electroacoustic absorber. J Sound Vib 2022;537:117201.
[29] De Bono E, Morell M, Collet M, Gourdon E, Ture Savadkoohi A, Ouisse M, et al. Model-inversion control to enforce tunable Duffing-like acoustical response on an electroacoustic resonator at low excitation levels. J Sound Vib 2024;570.
[30] Morell M, Gourdon E, Collet M, Ture Savadkoohi A, De Bono E, Lamarque C-H. Towards digitally programmed nonlinear electroacoustic resonators for low amplitude sound pressure levels: modeling and experiments. J Sound Vib 2024;584:118437.
[31] da Silveira Zanin CE, Labetoulle A, De Bono E, Gourdon E, Collet M, Ture Savadkoohi A. Experimental evidences of nonlinear programmable electroacoustic loudspeaker. Build Acoust 2023;30:249–63.

[32] De Bono E, Ponticelli D, De Rosa S, Petrone G, Ouisse M, Sadoulet-Reboul E, et al. Active impedance control optimization for attenuation of acoustic cavity modes. In: 30th AIAA/CEAS aeroacoustics conference (2024); 2024. p. 3195.
[33] Morell M, Collet M, Gourdon E, Savadkoohi AT, De Bono E. Experimental validation of the analytical modelling of a digitally created Duffing acoustic nonlinear oscillator at low amplitudes. Mech Ind 2025;26:2.
[34] Goodwin GC, Graebe SF, Salgado ME. Control system design, vol. 27. New Jersey: Prentice Hall; 2007.
[35] Morse PM, Ingard KU. Theoretical acoustics. Princeton University Press; 1986.
[36] Rienstra SW. Fundamentals of duct acoustics. Von Karman Institute Lecture Notes; 2015.
[37] Karkar S, De Bono E, Collet M, Matten G, Ouisse M, Rivet E. Broadband nonreciprocal acoustic propagation using programmable boundary conditions: from analytical modeling to experimental implementation. Phys Rev Appl 2019;12:054033.
[38] De Bono E, Collet M, Ouisse M. The advection boundary law in absence of mean flow: passivity, nonreciprocity and enhanced noise transmission attenuation. J Sound Vib 2024:118603.
[39] Billon K, De Bono E, Perez M, Salze E, Matten G, Gillet M, et al. In flow acoustic characterisation of a 2D active liner with local and non local strategies. Appl Acoust 2022;191:108655.
[40] De Bono E, Ouisse M, Collet M, Salze E, Mardjono J. A nonlocal boundary control, from plane waves to spinning modes control. In: Active and passive smart structures and integrated systems XVII, vol. 12483. SPIE; 2023. p. 74.
[41] de Bono E, Collet M, Salze E, Ouisse M, Gillet M, Lissek H, et al. Advection boundary law for sound transmission attenuation of plane and spinning guided modes. In: Forum acusticum; 2023.
[42] De Bono E, Collet M, Ouisse M. Breaking the limitations of local impedance noise control: passivity, and scattering performances of the advection boundary law. In: Active and passive smart structures and integrated systems XVIII, vol. 12946. SPIE; 2024. p. 302–11.
[43] De Bono E, Collet M, Ouisse M, Salze E, Volery M, Lissek H, et al. The advection boundary law in presence of mean-flow and spinning modes. In: Active and passive smart structures and integrated systems XVIII, vol. 12946. SPIE; 2024. p. 312–9.
[44] Billon K, Gillet M, Salze E, Volery M, De Bono E, Ouisse M, et al. Smart acoustic lining for UHBR technologies engine: from the design of an electroacoustic metasurface to experimental characterization under flow. In: Active and passive smart structures and integrated systems XVII, vol. 12483. SPIE; 2023. p. 72.
[45] De Bono E, Collet M, Billon K, Salze E, Lissek H, Volery M, et al. Smart acoustic lining for UHBR technologies engine part 1: design of an electroacoustic liner and experimental characterization under flow in rectangular cross-section ducts. In: 30th AIAA/CEAS aeroacoustics conference (2024); 2024. p. 3303.
[46] De Bono E, Collet M, Karkar S, Matten G, Ouisse M. Non-local boundary control for broadband non-reciprocal propagation: analytical demonstration and experimental validation. In: Euro-Mediterranean conference on structural dynamics and vibroacoustics; February 2020. p. 17–20.
[47] Billon K, De Bono E, Perez M, Salze E, Matten G, Gillet M, et al. Experimental assessment of an active (acoustic) liner prototype in an acoustic flow duct facility. In: Health monitoring of structural and biological systems XV, vol. 11593. International Society for Optics and Photonics; 2021. p. 84.
[48] Billon K, Collet M, Salze E, Gillet M, Ouisse M, Volery M, et al. 2D active liner experimental results in acoustic flow duct facility. In: Smart materials, adaptive structures and intelligent systems, vol. 86274. American Society of Mechanical Engineers; 2022:V001T03A001.
[49] De Bono E, Ouisse M, Collet M, Salze E, Lissek H, Volery M, et al. Programmable electroacoustic boundaries in acoustic waveguides: enhanced attenuation and non-reciprocal sound propagation. In: 10th ECCOMAS thematic conference on smart structures and materials; 2023.
[50] De Bono E, Collet M, Billon K, Salze E, Lissek H, Volery M, et al. Smart acoustic lining for UHBR technologies engine part 2: acoustic treatment at the intake of a scaled turbofan nacelle. In: 30th AIAA/CEAS aeroacoustics conference (2024); 2024. p. 3304.
[51] Beranek LL, Mellow T. Acoustics: sound fields and transducers. Oxford OX5 1GB, UK: Academic Press; 2012.
[52] De Bono E, Collet M, Karkar S, Matten G, Lissek H, Laurence T. Electroacoustic resonators: system identification and stabililty. In: 26th international congress on sound & vibration-ICSV26; 2019.
[53] Boulandet R, Lissek H, Karkar S, Collet M, Matten G, Ouisse M, et al. Duct modes damping through an adjustable electroacoustic liner under grazing incidence. J Sound Vib 2018;426:19–33.
[54] Pease RA. A comprehensive study of the howland current pump a comprehensive study of the howland current pump applications for the howland current pump AN-1515. Most 2008;29:12.
[55] Steele J, Green T. Tame those versatile current source circuits. Electron Des 1992;61.
[56] Rivet E, Karkar S, Lissek H. On the optimisation of multi-degree-of-freedom acoustic impedances of low-frequency electroacoustic absorbers for room modal equalisation. Acta Acust Acust 2017;103:1025–36.
[57] Salze E, Pereira A, Souchotte P, Regnard J, Gea-Aguilera F, Gruber M. New modular fan rig for advanced aeroacoustic tests-acoustic characterization of the facility. In: 25th AIAA/CEAS aeroacoustics conference; 2019. p. 2603.
[58] Pereira A, Salze E, Regnard J, Gea-Aguilera F, Gruber M. New modular fan rig for advanced aeroacoustic tests-modal decomposition on a 20″ UHBR fan stage. In: 25th AIAA/CEAS aeroacoustics conference; 2019. p. 2604.
[59] Brandstetter C, Paoletti B, Ottavy X. Compressible modal instability onset in an aerodynamically mistuned transonic fan. J Turbomach 2019;141:31004.
[60] Brandstetter C, Pages V, Duquesne P, Paoletti B, Aubert S, Ottavy X. Project PHARE-2—a high-speed UHBR fan test facility for a new open-test case. J Turbomach 2019;141:101004.
[61] Rodrigues M, Soulat L, Paoletti B, Ottavy X, Brandstetter C. Aerodynamic investigation of a composite low-speed fan for UHBR application. J Turbomach 2021;143:101004.
[62] Pagès V, Duquesne P, Aubert S, Blanc L, Ferrand P, Ottavy X, et al. Uhbr open-test-case fan ecl5/catana. Int J Turbomach Propuls Power 2022;7:17.
[63] Sree D, Stephens DB. Improved separation of tone and broadband noise components from open rotor acoustic data. Aerospace 2016;3:29.
[64] Nark DM, Jones MG, Sutliff DL. Improved broadband liner optimization applied to the advanced noise control fan. In: 20th AIAA/CEAS aeroacoustics conference; 2014. p. 3103.
[65] Figueroa-Ibrahim KM, Morris S, Ross M, Sutliff DL. Evaluation of radiated sound from the advanced noise control fan facility in an outdoor environment using ground microphones. In: AIAA propulsion and energy 2019 forum; 2019. p. 3825.
[66] Pereira A, Jacob MC. Modal analysis of in-duct fan broadband noise via an iterative Bayesian inverse approach. J Sound Vib 2022;520:116633.
[67] Glegg S, Devenport W. Aeroacoustics of low Mach number flows: fundamentals, analysis, and measurement. Academic Press; 2017.
[68] Betgen B, Galland MA. A new hybrid active/passive sound absorber with variable surface impedance. Mech Syst Signal Process 2011;25:1715–26.
[69] McAlpine A, Fisher MJ. On the prediction of “buzz-saw” noise in aero-engine inlet ducts. J Sound Vib 2001;248:123–49.
[70] Antoni J. Cyclostationarity by examples. Mech Syst Signal Process 2009;23:987–1036.